The Kinetochore Protein KNL-1 Regulates Actin Cytoskeleton Dynamics to Promote Dendrite Branching in Sensory Neurons

Mattie Green[1], Henrique Alves Domingos [1], Vasilis Ouzounidis[1], Cameron Finlayson[1], Bram Prevo[1] & Dhanya K. Cheerambathur [1*]

[1]Wellcome Centre for Cell Biology & Institute of Cell Biology, School of Biological Sciences, The University of Edinburgh, Edinburgh, EH9 3BF, UK

@: Corresponding author

Email: dhanya.cheerambathur@ed.ac.uk

ABSTRACT

Precise control of dendrite branching is essential for the formation of neural circuits, yet the mechanisms that regulate this process remain poorly understood. Here we show that the kinetochore protein KNL-1, known for its role in chromosome-microtubule coupling during mitosis, together with its binding partners, the KMN network, regulate dendritic branching in the *C. elegans* mechanosensory neuron, PVD, in a cell division independent manner. Neuron-specific degradation of KNL-1 results in excess dendrite branching and fusion events, predisposes PVD to age-dependent degeneration, and impairs animal sensory behavior. Surprisingly, these effects are not attributable to mis-regulation of the microtubule cytoskeleton. Instead, KNL-1 degradation alters the dynamics of F-actin, an established driver of dendrite branching. Epistasis analysis shows that KNL-1 counters the activity of the RacGEF TIAM-1, a downstream effector of dendrite guidance receptors. These findings establish that the microtubule coupling KMN network promotes dendrite branching by regulating the actin cytoskeleton and provide insight into how the cytoskeleton shapes dendritic architecture.

KEY WORDS: cytoskeleton, actin, microtubule, kinetochore, dendrite, neurodevelopment, dendrite morphogenesis, dendrite arborization, KNL-1, TIAM-1, PVD neuron

INTRODUCTION

Neurons have specialized compartments for transmitting information, including dendrites, which receive & integrate signals, and axons, which propagate them. The shape, size and trajectory of dendritic and axonal processes determines how a neuron communicates and functions. Dendrites display diverse shapes and complex branching patterns that are unique to neuronal types[1]. The dendrite arborization pattern defines how input signals are distributed and integrated, ultimately shaping the functional properties of neurons and their connectivity within the neural circuits. Proper development and organization of dendritic arbors is therefore crucial for establishing the neural circuits, which regulate animal behavior. Notably, alterations in dendrite morphology and organization are associated with several neurodevelopmental & neurodegenerative disorders [2].

Dendrite morphogenesis initiates when extrinsic guidance cues interact with specific cell surface receptors on the neuron and activate intracellular signaling pathways that trigger cytoskeletal rearrangements to enable dendrite growth and branching [2]. The Rho family of GTPases (Cdc-42, Rac1, and RhoA) are key downstream effectors of the guidance cues during dendrite development[3–6]. Rho GTPases influence dendrite arborization by regulating actin filament assembly and the formation of actin structures such as filopodia and lamellipodia. During dendrite outgrowth, dynamic actin filaments form a network of lamellipodial and filopodial protrusions that guide and propel the growth cone. Dendritic arborization occurs when filopodia emerge from preexisting branches and undergo extension and retraction until they become stabilized[7]. Consequently, dendrite arbor growth and stabilization entail extensive actin remodeling and careful coordination between actin growth states and structures. Various actin regulators, including F-actin nucleators modulators of F-actin dynamics, have been shown to affect dendrite morphogenesis [8,9] . However, it is unclear how the activity of different actin regulators is coordinated and controlled spatially & temporally by the Rho GTPases to generate a specific dendrite pattern.

The microtubule cytoskeleton is also critical for dendrite morphogenesis. Microtubules provide structural support for dendrites and serve as tracks to transport key building materials and organelles. Mutations in molecular motors that affect transport severely impair dendrite morphology, and loss of microtubules-associated proteins result in dendrite development defects[10–14]. In addition, microtubule nucleators are found at branch points of developing dendrites, where they organize microtubule arrays to regulate branching[15]. Studies on the role of microtubules in dendritic spines, small actin-rich protrusions on dendrite branches that are sites of high synaptic activity, have shown that dynamic microtubules enter the actin-rich spines in a synaptic-activity-dependent manner and that this is facilitated by actin cytoskeleton remodeling[12,16,17]. Thus, a crosstalk between the two cytoskeletal structures appears to exist within dendrites, but its molecular basis remains elusive.

Recent studies have revealed that kinetochore proteins, which connect chromosomes to dynamic spindle microtubules in dividing cells, also play an unexpected post-mitotic role during neurodevelopment. The conserved 10-subunit Knl1 complex/Mis12 complex/Ndc80 complex (KMN) network, which serves as the primary chromosome-microtubule coupler[18,19], is enriched along developing dendrites of *C. elegans* sensory neurons and in the synapses and axons of *D. melanogaster* neurons [20,21]. Depletion of any KMN component in *C. elegans* sensory neurons results in dendrite growth defects, indicating that KMN function is critical for dendrite development. Knockdown of Mis12 causes dendrite branching defects in *D. melanogaster* embryonic sensory neurons and increases filopodial protrusions in dendrites of rat hippocampal neurons, underscoring the importance of the Mis12 complex for proper dendrite formation. Moreover, kinetochore proteins promote dendrite regeneration of *D.*

melanogaster sensory neurons, highlighting their involvement in the maintenance of dendrite morphology [22].

The mechanisms by which kinetochore proteins contribute to dendrite development and maintenance is not understood, but some observations imply that microtubule binding activity is important [20,22]. The neuronal function of KMN network in *C. elegans* sensory neurons depends on the microtubule coupling interface within the Ndc80 complex. Additionally, knockdown of kinetochore proteins in *D. melanogaster* sensory neurons increases the number of microtubule plus ends in dendrites, suggesting a role in the regulation of microtubule dynamics[22].

Our previous characterization of the KMN network's post mitotic role in neurons focused on dendrite extensions of the *C. elegans* amphid sensory neuron bundles, which consist of 12 dendrites from 12 neurons[20]. This precluded a detailed analysis of cellular structures within dendrites at the single-neuron level. To overcome this limitation, we have examined the role of KNL-1 during dendrite branching of the mechanosensory neuron PVD. Dendrite development in PVD is stereotypical and invariant, and its cytoskeletal organization is well characterized, making it a good system to investigate kinetochore protein function. In this study we demonstrate that KNL-1 is concentrated in the extending dendrites processes and at branch points, and that PVD-specific degradation of KNL-1 perturbs higher order branch formation, leading to behavioral defects and premature neurodegeneration. Surprisingly, KNL-1 degradation does not affect microtubule organization or dynamics, but instead up-regulates F-actin assembly in the cell body and primary dendrites. We show that KNL-1 acts antagonistically to the RacGEF TIAM-1, the downstream effector of dendrite branching cues. Thus, the kinetochore protein KNL-1 contributes to the dendrite guidance pathway through regulation of the neuronal actin cytoskeleton.

RESULTS

KNL-1 localizes to developing dendrites in the PVD neuron

The PVD neuron in *C. elegans* is a type of mechanosensory neuron located between the body wall muscle and the epidermis of the animal. A unique feature of the PVD is the highly arborized dendrites that extend throughout the animal's body. **(Figure 1A)**. PVD dendrites form a distinctive branching pattern composed of non-overlapping repeating units called "menorahs", which are important for integrating and processing sensory inputs **(Figure 1A)**[23]. PVD dendrite branches are established during the larval stages and the branching follows a stereotypical developmental program that begins at the late L2 larval stage and concludes by the late L4 larval stage **(Figure S1A)**. To visualize the localization of the kinetochore protein KNL-1 in the PVD neuron, we used a split-GFP system[24]. The N-terminus of KNL-1 was fused to 7 copies of the β11 strand of GFP at the endogenous locus, and the complementing GFP 1-10 was expressed under a PVD-specific promoter. The cell body of PVD is located near the animal tail, and two primary (1°) dendrites extend from the cell body towards the anterior and posterior. KNL-1 was enriched in the cell body and along the extending 1° dendrites at the L2 larval stage **(Figure 1B)**. During the L3 and L4 stages, higher order branches develop from the 1° dendrite to generate the distinctive menorah shape. KNL-1 signal persisted along the 1° dendrites in the L3 and L4 stages but became more punctate **(Figure S1B)**. We also observed discrete KNL-1 puncta at the base of branch points of 2° dendrite and 3° dendrites, as well as along the newly formed 3° dendrites **(Figures 1C, 2D & S1B-D)**. These results indicated that KNL-1 may play a role in PVD dendrite formation.

KNL-1 functions cooperatively with the KMN network to restrict dendritic branching

To investigate the function of KNL-1 in the PVD neuron, we utilized an auxin inducible degron (AID) to selectively degrade KNL-1 in the PVD neuron (KNL-1 degrader). We fused an AID peptide sequence along with GFP to KNL-1 at the endogenous locus and expressed the plant specific F-box protein TIR1 under PVD-specific promoters **(Figure 2A)**[25,26]. To degrade KNL-1, we synchronized the worms as L1 larvae and exposed them to auxin at the L2 stage when PVD development is initiated **(Figure S2A)**. We observed a significant reduction in GFP::KNL-1 signal from the PVD cell body at the L2 stage **(Figure 2A)**. To assess the effect of KNL-1 degradation on PVD development, we visualized dendrite morphology in L4 larvae by expressing a plasma membrane (pleckstrin homology domain, PH) marker. Both control and KNL-1 degrader neurons exhibited proper extension of their 1° dendrites**.** However, we observed a significant disruption of the higher-order branching pattern following KNL-1 degradation **(Figures 2B & S2F)**. Menorahs consist of dendrite branches that are arranged at right angles with respect to each other. Specifically, each menorah contains a 2° dendrite that branches off at a right angle from the 1° dendrite, which then gives rise to an orthogonal 3° branch that forms the base of menorah. Finally, several smaller 4° dendrites emerge at right angles to the 3° dendrite to complete the menorah. The number of 2° dendrite branches was not significantly different between control and KNL-1 degrader neurons **(Figure S2B).** However, KNL-1 degrader neurons exhibited an increased number of 4° dendrite branches **(Figure 2C)**, an increased number of fusion events between 3° dendrites **(Figure 2D)**, and an increased number of ectopic neurites originating from the 1° dendrites **(Figure S2C)**.

We next overexpressed KNL-1 in the PVD neuron by generating extrachromosomal arrays that contain multiple copies of transgenic KNL-1::GFP under a PVD-specific promoter. Compared to control animals that contained a GFP-expressing plasmid in the array, animals with KNL-1::GFP arrays exhibited a decrease in higher-order branching. Specifically, the number of 2° and 4° dendrite branches were significantly reduced **(Figures 2H, 2I & S2J)**. We conclude that PVD-specific degradation and overexpression of KNL-1 have opposite effects on higher-order dendritic branching.

We also investigated the effect of degrading the Mis12 and the Ndc80 complexes within the KMN network on PVD branching. Degradation of KNL-3 (a component of the Mis12 complex) or Ndc80 disrupted PVD dendrite architecture in a similar manner to KNL-1 degradation **(Figure S2E-I)**. Taken together, these results reveal that PVD-localized KNL-1 functions in the context of the KMN network to restrict dendritic branching. We conclude that the kinetochore-microtubule coupling machinery has a crucial role in ensuring proper PVD dendrite arborization.

KNL-1 regulates the dynamics and stability of dendrite branches

A prominent effect of KNL-1 degradation is the fusion of neighboring menorahs resulting from the merging or overlap of 3° dendrites **(Figure 2D)**. In control neurons, 3° dendrites of neighboring menorahs do not overlap with each other because they quickly retract after contacting each other. The aberrant fusion observed following KNL-1 degradation and the presence of GFP::KNL-1 puncta along the 3° dendrite and at branch points within the menorah **(Figures 1C & S2I)** suggests that KNL-1 plays a role in resolving contacts between the growing tips of neighboring 3° dendrites. To understand how KNL-1 contributes to the spatial separation of menorahs, we tracked the growth dynamics of 3° dendrites. Consistent with previous studies [23,27], 3° dendrites of neighboring menorahs retracted within 5-10 min of mutual contact in control neurons **(Figure 2E, 2G)**. In KNL-1 degrader neurons, the frequency with which neighboring 3° dendrites established contact remained unchanged **(Figure S2D)** but contact duration was longer **(Figure 2G)**. The presence of persistent contacts after KNL-1 degradation resulted in a higher frequency of unresolved fusions, indicating that KNL-1 function ensures timely retraction of 3° dendrites during menorah formation **(Figure 2F)**. These observations suggest that KNL-1 regulates the dynamics and stability of dendrite branches to establish the highly ordered branching pattern of PVD neurons.

KNL-1 degradation impairs function and lifespan of the PVD neuron

As KNL-1 function is essential for proper dendrite arborization in the PVD neuron, we next examined the sensory behavior of KNL-1 degrader animals. Proprioception, awareness of body position and movement, is attributed to PVD dendrites that sense mechanical stimuli and provide feedback to the body wall muscles to generate a stereotypical sinusoidal locomotory pattern **(Figure 3A)**. To determine the body posture of animals, we visualized their movement on food and measured wavelength and amplitude of their sinusoidal tracks. As a positive control, we used animals lacking DMA-1, a transmembrane receptor that is essential for PVD dendrite formation. KNL-1 degrader animals showed reduced amplitudes and wavelengths, indicating that degradation of KNL-1 in the PVD neuron impairs proprioception **(Figures 3A - C)**.

Analysis of PVD morphology at the L4 stage revealed that dendrites of KNL-1 degrader neurons contained more bead-like structures compared to control neurons **(Figures 3D, 3E)**. Beading is implicated in age-dependent decline of PVD dendrites [28], and substantial beading does not appear until late into adulthood (Day 6) in control neurons. The presence of substantial beading at the L4 stage suggested that KNL-1 degrader neurons degenerate prematurely. Age-dependent degeneration of PVD dendrites is mediated by the autophagy pathway [28], and autophagosomes marked by mScarlet-I::LGG-1 were enriched in dendrites of KNL-1 degrader neurons at the day 1 adult stage **(Figure 3F, 3G)**. These observations suggest that KNL-1 degradation predisposes the PVD neuron to premature ageing.

KNL-1 degradation does not perturb PVD polarity, microtubule organization, or microtubule dynamics

The canonical role of KMN network proteins is to stabilize the interactions between chromosomes and microtubules during chromosome segregation. Microtubule function and stability are also critical for the establishment and maintenance of neuronal polarity in the PVD neuron [11,29,30]. Therefore, we hypothesized that KNL-1 could affect PVD dendrite branching by regulating the underlying microtubule architecture and neuronal polarity. To determine whether KNL-1 degradation impacts PVD polarity, we assessed the distribution of RAB-3, a small GTPase associated with synaptic vesicles, and DMA-1, which localizes exclusively to dendrites **(Figure 4A)**. We observed no change in the distribution of either RAB-3 or DMA-1 following KNL-1 degradation, indicating that PVD polarity remains intact **(Figure 4B 4C & S3A, S3B)**.

Next, we investigated whether KNL-1 degradation impacts the distribution, dynamics, or stability of microtubules in the 1° anterior dendrite. To monitor microtubule orientation and dynamics we imaged the microtubule plus end-tracking protein $EB1^{EBP-2}$, which binds to growing microtubule plus ends. $EB1^{EBP-2}$::GFP was expressed under a PVD-specific promoter, and its trajectories were followed by time-lapse imaging in L4 larvae **(Figure 4D)**. In control neurons, the majority of the $EB1^{EBP-2}$::GFP puncta moved towards the cell body, which is consistent with previous observations [10,31] that within the 1° anterior dendrite microtubules are oriented with their minus end distal **(Figure 4D & 4E)**. There was no significant difference in the direction of movement, velocity, or frequency of $EB1^{EBP-2}$::GFP comets in KNL-1 degrader neurons **(Figure 4D, 4E & S3D, S3E)**. Thus, KNL-1 does not contribute to the orientation, distribution, or dynamics of microtubule plus ends within PVD dendrites.

We also examined tubulin distribution and microtubule stability in PVD dendrites by expressing an α-tubulin GFP-fusion protein. GFP::TBA-1 is enriched in 1° dendrites and is not detectable in higher-order dendrite branches of control animals, and this distribution was not affected by KNL-1 degradation **(Figure S3C)**. To assess the stability of microtubules, we performed Fluorescence Recovery After Photobleaching (FRAP) experiments on microtubules labeled with endogenous GFP::TBA-1 using the split-gfp system **(Figure 4F)**. After KNL-1 degradation, microtubules within the 1° anterior dendrite recovered to a similar extent (~20%) and with the same kinetics as microtubules in control neurons **(Figure 4F & S3F)**. Recovery kinetics indicate that microtubules in the 1° anterior dendrite are largely stable, and that microtubule stability is not impaired by KNL-1 degradation. Overall, these experiments indicate that altered neuronal polarity or perturbed microtubule organization and dynamics are unlikely to account for the striking effect of KNL-1 loss on PVD dendritic branching and consequent impairment of PVD neuron function and lifespan.

KNL-1 limits F-actin assembly and dynamics in the PVD cell body and dendrites

During our analysis of PVD morphology, we noticed that the cell body in KNL-1 degrader animals was enlarged and deformed **(Figure 5A, 5B)**, suggestive of defects associated with the actin cytoskeleton. To visualize the actin cytoskeleton during PVD dendrite branching, we generated a strain expressing Lifeact, the actin binding peptide of the yeast protein Abp140, fused to mKate2 under a PVD-specific promoter. We imaged actin and the plasma membrane of the PVD neuron at the L4 stage, when 4° dendritic branches are beginning to form. In control neurons, Lifeact::mKate2 signal is enriched in the 3° and 4° dendrites compared to the 1° dendrites and the cell body, consistent with previous observations [32,33] that newly formed dendrites show a higher concentration of F-actin **(Figure 5C)**. In KNL-1 degrader neurons, Lifeact::mKate2 signal intensity in the cell body and proximal 1° dendrites was significantly increased **(Figure 5C),** and close examination revealed prominent F-actin cables in the cell body of KNL-1 degrader neurons **(Figure 5D-G & S4A-C)**. These results suggest that degradation of KNL-1 during PVD development results in increased F-actin levels.

To assess F-actin dynamics, we performed FRAP in the 1° anterior dendrite. In both control and KNL-1 degrader neurons, recovery of Lifeact::mKate2 signal was slow suggesting a low turnover rate for F-actin. However, the extent of recovery was significantly lower in KNL-1 degrader neurons (8% vs. 14% in controls) indicative of a higher fraction of stable F-actin structures **(Figure 5H, 5I)**.

Consistent with a role for KNL-1 in regulating F-actin dynamics, we found that KNL-1 influences the dynamics of filopodial protrusions from 1° dendrites. 2° dendrite branches initiate when several actin-rich filopodial like projections extend orthogonally from the 1° dendrite. Most of these filopodia undergo several cycles of extension and retraction until a subset of projections stabilize to form the 2° dendrites **(Figure S4D)**. The number of filopodial protrusions from 1° dendrites was significantly increased in KNL-1 degrader neurons **(Figure 5J, 5K & S4D)**. Unlike the filopodial outgrowths in control dendrites, which extend orthogonally for a short period, protrusions in KNL-1 degrader dendrites had a longer lifetime and arbitrary trajectories, often running parallel to 1° dendrites **(Figure 4SD)**. These observations suggest that KNL-1 plays a critical role in regulating filopodial generation and dynamics in 1° dendrites.

KNL-1 acts antagonistically to the RacGEF TIAM-1 to promote dendrite branching

Since KNL-1 regulates F-actin and dendrite branch dynamics as well as menorah formation, we investigated how it connects with the molecular pathway that controls F-actin remodeling and dendrite branching. Dendrite branching is driven by actin polymerization, which is triggered by Rho family GTPases activated in response to guidance cues [9]. Specifically, the adhesion molecules L1CAM/SAX-7 and MNR-1 in the epidermis interact with DMA-1/LRR, the dendrite guidance receptor on the surface of the PVD neuron to initiate the formation of 3° and 4° branches . Within the PVD neuron, DMA-1 in conjunction with HPO-30, the claudin-like transmembrane protein, functions as a scaffold for the RacGEF TIAM-1 and the Arp2/3 complex activator WRC (Wave Regulatory Complex) to promote actin assembly and drive dendrite branching **(Figure 6A)**. To determine whether KNL-1 acts in the DMA-1-mediated F-actin assembly pathway, we performed epistasis analysis of PVD-specific KNL-1 degradation with mutants in the *dma-1*-mediated branching pathway. Deletion of *dma-1* results in complete loss of branching and menorah formation. Combining KNL-1 degradation with a *dma-1Δ* mutant resulted in a similar phenotype as *dma-1Δ* alone, suggesting that KNL-1 functions downstream of DMA-1.

We next tested the genetic interaction between KNL-1 and TIAM-1. TIAM-1 is essential for higher order branching, as *tiam-1Δ* PVD neurons exhibit “immature” menorahs that lack 4° branches **(Figure 6B, 6C)**. KNL-1 degradation in the PVD suppressed the branching defects observed in *tiam-1Δ* animals and led to complete restoration of the menorahs and the 3° and 4° branch counts **(Figure 6B-D)**. This suggests that KNL-1 degradation compensates for the loss of *tiam-1* by promoting dendrite branching. Additionally, the menorah fusion defects observed in KNL-1 degrader neurons were reduced in *tiam-1Δ* animals, indicating that KNL-1 and TIAM-1 have opposing effects on menorah formation **(Figure 6E)**.

TIAM-1 is a RacGEF proposed to locally recruit active Rac to initiate F-actin assembly. Interestingly, in addition to the suppression of branching defects, *tiam-1Δ* also suppressed the cell body shape defects of KNL-1 degrader neurons **(Figure 6F, 6G)**. Consistent with this rescue, we found that F-actin levels in the cell body were no longer increased when KNL-1 was degraded in the *tiam-1Δ* background **(Figure 6G-I)**. Given that *tiam-1Δ* rescued F-actin levels in KNL-1 degrader neurons, we were surprised to find that *tiam-1Δ* on its own increased F-actin levels to a similar extent as KNL-1 degradation **(Figure 6G-I)**. This indicates that TIAM-1 does not solely function as a GEF that promotes actin polymerization, and further work will be necessary to understand the role of TIAM-1 in F-actin regulation and its epistatic effect with KNL-1 degradation. Overall, these results demonstrate that KNL-1 and TIAM-1 act antagonistically to modulate actin polymerization dynamics to promote the branching and proper patterning of dendrite architecture of the PVD neuron.

DISCUSSION

Dendrite morphogenesis is a highly orchestrated process that requires precise regulation of the actin and microtubule cytoskeleton. Various effectors of cytoskeletal remodeling in dendrites have been identified, but how effector functions are coordinated to generate the unique dendrite pattern of each neuron remains largely undefined. Taking advantage of the unique morphology of the PVD neuron and a PVD-specific protein-degradation system, we show that the kinetochore component KNL-1 facilitates dendrite arborization, and that it does so in the context of the KMN network, the microtubule-coupling machine that drives chromosome segregation during cell division.

KNL-1 degradation does not appreciably affect microtubule organization or growth dynamics in PVD dendrites, nor does it affect PVD polarity, which is consistent with observations in *D. melanogaster* sensory neurons[22]. KNL-1 degradation also has no effect on the abundance of EB1-marked microtubule plus ends, which contrasts with the increased number of EB1 comets observed after knockdown of Ndc80 and Mis12 subunits in *D. melanogaster* neurons. KNL-1 function therefore appears to differ significantly from that of other known microtubule-associated proteins in PVD, whose inhibition primarily affects neuronal polarity or microtubule orientation and stability [10,29,30,34].

Taken together, our results argue against the idea that KNL-1 facilitates dendrite branching through regulation of the microtubule cytoskeleton. Instead, we unexpectedly found that KNL-1 degradation increases F-actin levels in the cell body and primary dendrites and promotes formation of filopodial protrusions from primary dendrites, which suggested to us that KNL-1 might regulate actin filament dynamics. Furthermore, the observed increase in filopodial protrusions after Mis12 knockdown in rat hippocampal neurons is consistent with the idea that other components of the KMN network may also affect the actin cytoskeleton[21]. It remains to be determined whether KNL-1's effect on actin requires association of the KMN network with microtubules. We note, however, that KNL-1 does not appear to be specifically enriched at microtubule-based structures (data not shown), and that fluorescence microscopy suggests microtubules are absent in 3° and 4° dendrites, where KNL-1 presumably acts during dendrite branching [11,35].

Recent studies suggest that dendrite branching results from a balance of F-actin-dependent dendrite growth and retraction, and our time lapse analysis shows that KNL-1 degradation primarily inhibits branch retraction [27,35]. At the molecular level, dendrite branching in PVD is driven by synergistic interaction between DMA-1, the transmembrane guidance receptor, and HPO-30, the claudin superfamily member[32,33]. DMA-1 & HPO-30 are thought to independently recruit the WAVE regulatory complex (WRC) to promote Arp2/3 mediated assembly of branched F-actin networks, with DMA-1 recruiting WRC via the RacGEF TIAM-1, and HPO-30 recruiting WRC directly through its C-terminal domain. TIAM-1 is essential to form 3° & 4° branching[32,33], and we show that KNL-1 degradation rescues the branching defects observed in *tiam-1Δ*. Moreover, the KNL-1 degradation phenotype in PVD is similar to that of TIAM-1 or DMA-1 overexpression. This suggests that KNL-1 functions in the DMA-1 pathway and promotes dendrite branching by antagonizing TIAM-1-mediated F-actin assembly. A parsimonious explanation would be that KNL-1 counters the GEF activity of TIAM-1. However, this is contradicted by the observation that the GEF activity of TIAM-1 is not essential for dendrite branching.

An emerging view is that a balance between linear and branched actin filaments underlies the transition from extension to retraction of the growing 3° dendrites[35]. Interestingly, previous work showed that Formin, a nucleator of linear actin filaments, is enriched at kinetochores of human cultured cells and contributes to the stability of kinetochore-attached microtubules during mitosis in mammalian cells and during meiosis in oocytes[36–38]. Moreover, a recent study showed that F-actin cables generated by Formin and Spire, another nucleator of linear actin filaments, interact with kinetochores during porcine oocyte meiosis[39]. Given this close link between kinetochores and Formin, an attractive hypothesis to be tested in the future is that the PVD-localized KMN network regulates linear F-actin assembly during dendrite outgrowth, thereby ensuring the balance between linear and branched F-actin filaments required for proper dendrite arborization.

ACKNOWLEDGMENTS

We thank Reto Gassmann and Rebecca Green for comments on the manuscript. This work is supported by a Sir Henry Wellcome Postdoctoral Fellowship (215925) to B.P. and a Sir Henry Dale Fellowship (208833) to D.K.C. Imaging was performed in Centre Optical Instrumentation Laboratory (COIL), which is supported by a Core Grant (203149) to the Wellcome Centre for Cell Biology at the University of Edinburgh. Some strains were provided by the CGC, which is funded by NIH Office of Research Infrastructure Programs (P40 OD010440)

DECLARATION OF INTERESTS

The authors declare no competing interests.

Figure 1

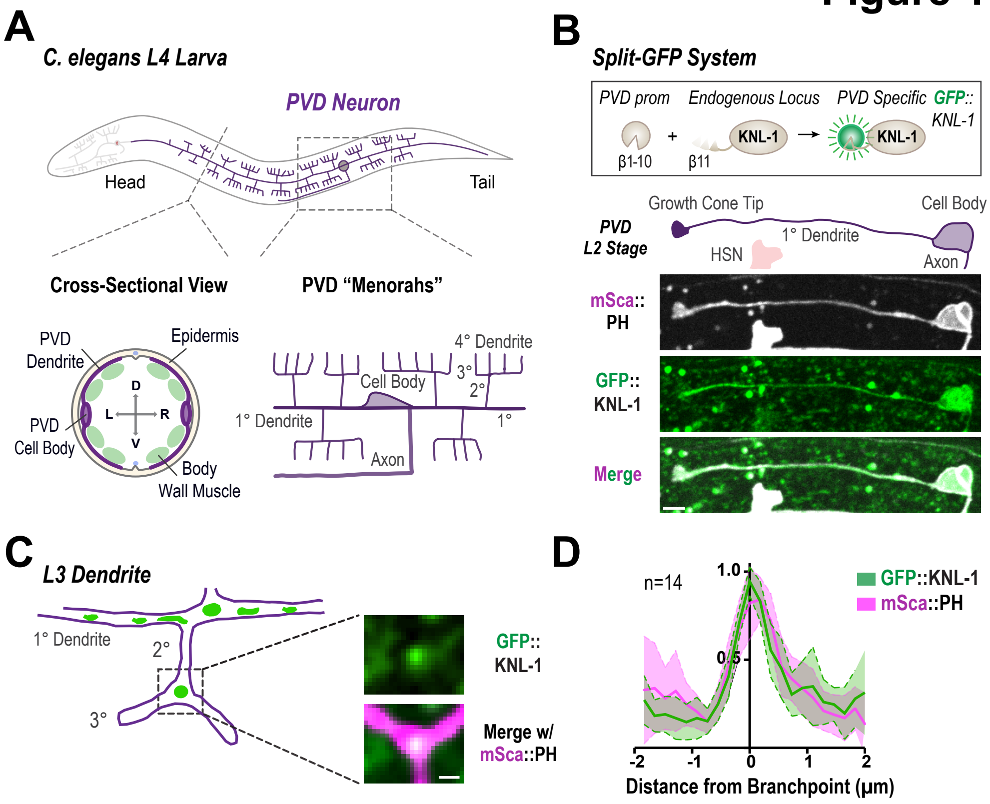
A
C. elegans L4 Larva
PVD Neuron
Head
Tail
Cross-Sectional View
PVD "Menorahs"
PVD Dendrite
Epidermis
D
L
R
V
PVD Cell Body
Body Wall Muscle
4° Dendrite
Cell Body
3°
2°
1° Dendrite
1°
Axon
B
Split-GFP System
PVD prom
Endogenous Locus
PVD Specific GFP:: KNL-1
β1-10
β11
KNL-1
KNL-1
Growth Cone Tip
Cell Body
PVD L2 Stage
1° Dendrite
HSN
Axon
mSca:: PH
GFP:: KNL-1
Merge
C
L3 Dendrite
1° Dendrite
2°
3°
GFP:: KNL-1
Merge w/ mSca::PH
D
n=14
1.0
0.5
GFP::KNL-1
mSca::PH
-2
-1
0
1
2
Distance from Branchpoint (μm)

Figure 1. KNL-1 localisation in the PVD neuron.

(A) Schematic of the PVD neuron at the L4 larval stage. The left inset cartoon shows a cross-sectional view of PVD between the epidermis and body wall muscle. The right inset illustrates the discrete "menorah"-like dendrite branching pattern of the PVD neuron. **(B)** Localization of GFP::KNL-1 expressed specifically in PVD neuron using a split-GFP system. The image represents an L2 stage PVD neuron which has begun to extend its anterior dendrite. Scale bar, 5μm. **(C)** An example, with a schematic, of GFP::KNL-1 localizing at the developing branch points in an L3 stage PVD dendrite. Scale Bar, 1μm. **(D)** Quantification of GFP::KNL-1 at the intersections of 2° and 3° dendrites as shown in (C).

Figure 2

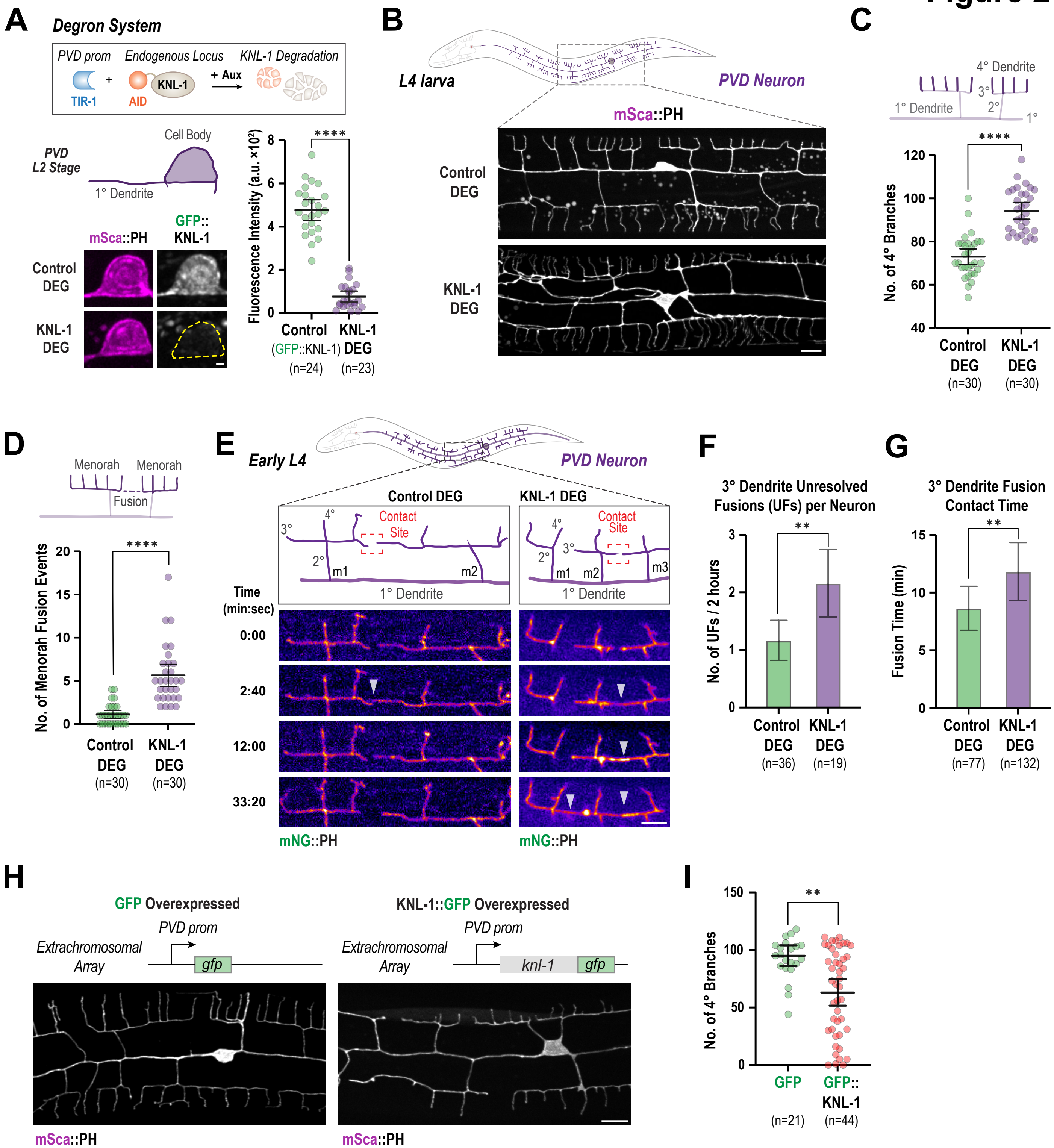
A
Degron System
PVD prom
Endogenous Locus
KNL-1 Degradation
TIR-1
AID
KNL-1
+ Aux
PVD L2 Stage
Cell Body
1° Dendrite
mSca::PH
GFP:: KNL-1
Control DEG
KNL-1 DEG
Fluorescence Intensity (a.u. x10²)
****
Control (GFP::KNL-1)
KNL-1 DEG
(n=24)
(n=23)
B
L4 larva
PVD Neuron
mSca::PH
Control DEG
KNL-1 DEG
C
4° Dendrite
3°
2°
1° Dendrite
1°
No. of 4° Branches
****
Control DEG (n=30)
KNL-1 DEG (n=30)
D
Menorah
Menorah
Fusion
No. of Menorah Fusion Events
****
Control DEG (n=30)
KNL-1 DEG (n=30)
E
Early L4
PVD Neuron
Control DEG
KNL-1 DEG
Contact Site
1° Dendrite
m1
m2
m3
Time (min:sec)
0:00
2:40
12:00
33:20
mNG::PH
F
3° Dendrite Unresolved Fusions (UFs) per Neuron
No. of UFs / 2 hours
**
Control DEG (n=36)
KNL-1 DEG (n=19)
G
3° Dendrite Fusion Contact Time
Fusion Time (min)
**
Control DEG (n=77)
KNL-1 DEG (n=132)
H
GFP Overexpressed
KNL-1::GFP Overexpressed
PVD prom
Extrachromosomal Array
gfp
knl-1
mSca::PH
I
No. of 4° Branches
**
GFP (n=21)
GFP:: KNL-1 (n=44)

Figure 2. KNL-1 is required for proper dendrite branching of the PVD neuron.

(A) Approach used to degrade endogenously tagged AID::KNL-1 in the PVD neuron (top). Images below show loss of GFP::KNL-1 signal in presence of PVD-specific Tir1 transgene & auxin. The plot on the right shows the mean fluorescence intensity of the GFP signal in the cell body for control & KNL-1 DEG. Scale bar, 1μm. **(B)** Images of PVD dendrite organization in the control (top) & KNL-1 DEG (bottom). Scale bar, 10μm. **(C&D)** Quantification of PVD dendrite organization in terms of 4° branch count and fusion between menorahs in control & KNL-1 DEG. **(E)** Stills from time-lapse imaging of 3° dendrite branch dynamics in control & KNL-1 DEG animals. White arrow heads denote fusion events between two adjacent menorahs. Scale bar, 5μm. **(F)** Quantification of the number of fusion events between 3° dendrites of two adjacent menorahs that remained unresolved during the time lapse. n corresponds to the total number of animals analyzed in each condition. **(G)** Quantification of time spent in contact by 3° dendrites of two adjacent menorahs. n corresponds to the total events analyzed in control animals and KNL-1 DEG animals. **(H)** Images of PVD in control (GFP) (left) & KNL-1 GFP overexpressing animals (right). Scale bars, 10μm. **(I)** Quantification of the number of 4° branches in the PVD in control (GFP) and KNL-1::GFP overexpressing animals.

Figure 3

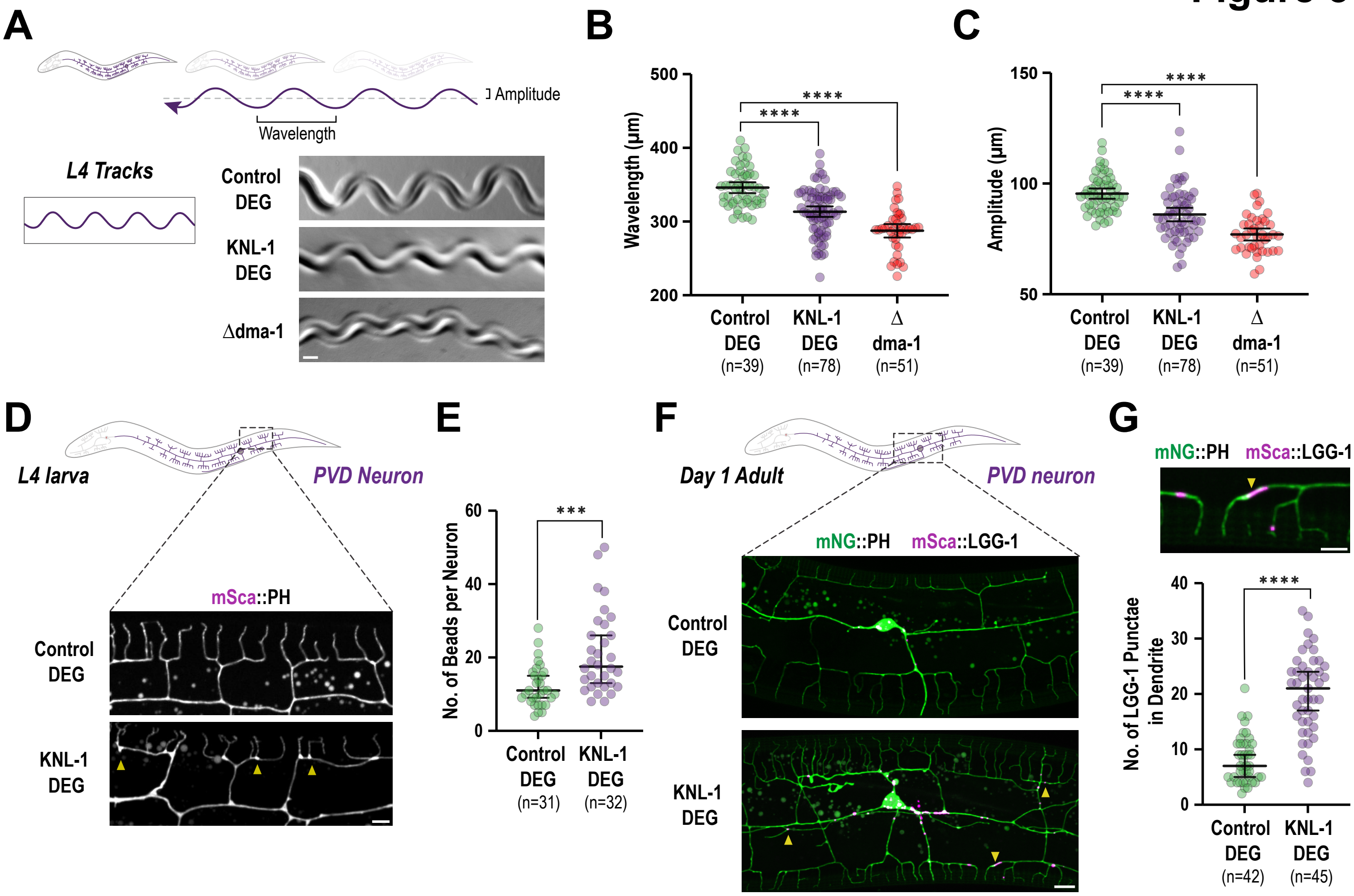
A
Amplitude
Wavelength
L4 Tracks
Control DEG
KNL-1 DEG
Δdma-1
B
Wavelength (µm)
500
400
300
200
****
****
Control DEG (n=39)
KNL-1 DEG (n=78)
Δ dma-1 (n=51)
C
Amplitude (µm)
150
100
50
****
****
Control DEG (n=39)
KNL-1 DEG (n=78)
Δ dma-1 (n=51)
D
L4 larva
PVD Neuron
mSca::PH
Control DEG
KNL-1 DEG
E
No. of Beads per Neuron
60
40
20
0
***
Control DEG (n=31)
KNL-1 DEG (n=32)
F
Day 1 Adult
PVD neuron
mNG::PH mSca::LGG-1
Control DEG
KNL-1 DEG
G
mNG::PH mSca::LGG-1
No. of LGG-1 Punctae in Dendrite
40
30
20
10
0
****
Control DEG (n=42)
KNL-1 DEG (n=45)

Figure 3. KNL-1 is important for proprioceptive behavior and PVD neuron maintenance. **(A)** Proprioception behavior analysis**.** Representative tracks of animals in indicated conditions**.** The wild type control worms form sinusoidal tracks. Scale bar, 20µm **(B&C)** Quantification of the wavelength and amplitude of the tracks by animals in indicated conditions. **(D)** Images of PVD dendrite organization in the control (top) & KNL-1 DEG (bottom) animals. Yellow arrowhead indicates the bead-like blebs seen with membranes. Scale bar, 5µm. **(E)** Quantification of the bead-like blebs in control and KNL-1 DEG animals. **(F)** Autophagosomes labeled with the marker mScarlet-I::LGG-1 overlaid with membrane (mNeonGreen::PH) in control & KNL-1 DEG adult animals. Yellow arrowheads indicate the appearance of LGG-1 puncta along the dendrites. Scale bar, 10µm. **(G)** Quantification of mScarlet-I::LGG-1 puncta in the dendrites in control & KNL-1 DEG animals. Yellow arrowhead indicates an LGG-1 puncta. Scale bar, 5µm.

Figure 4

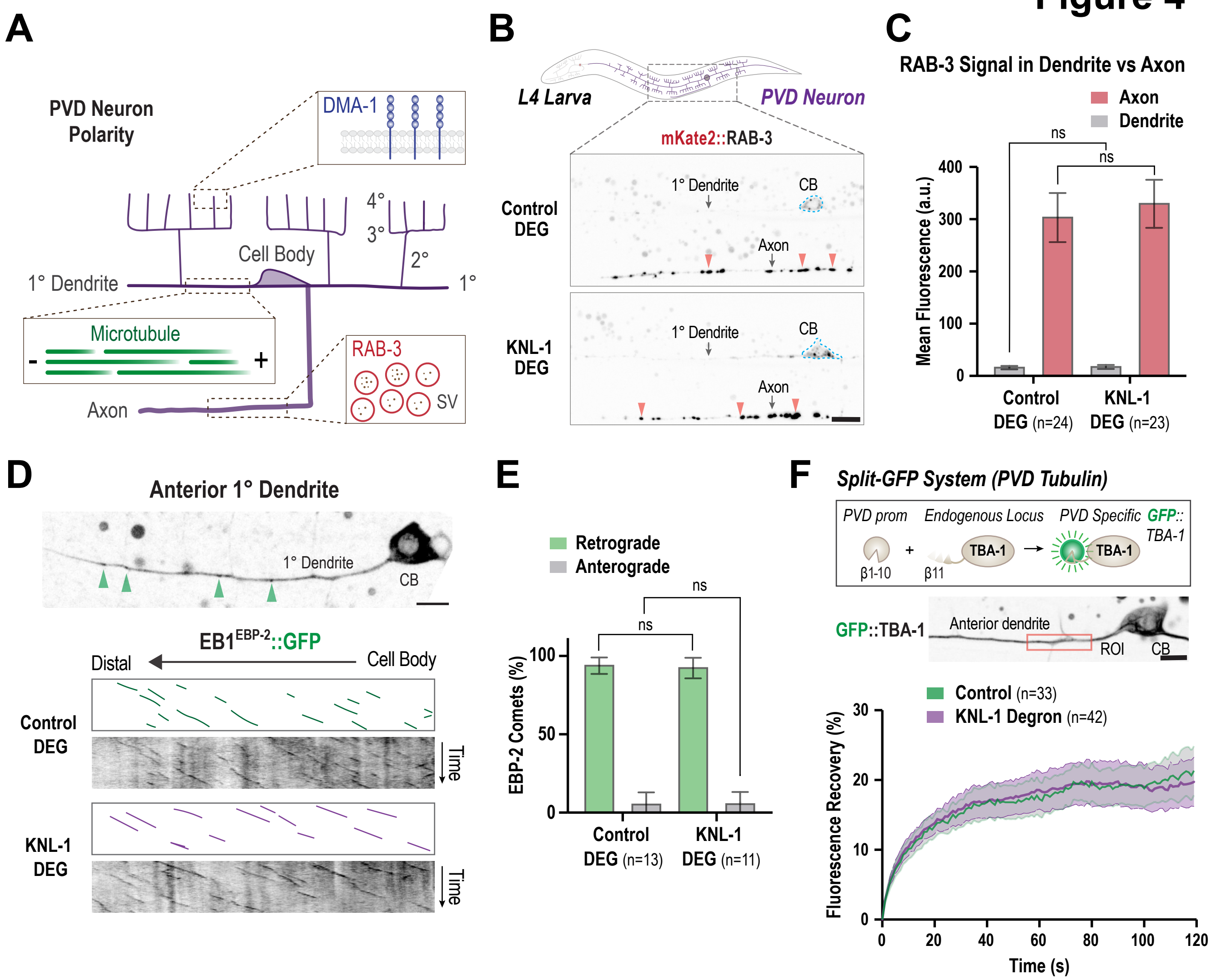
A
PVD Neuron Polarity
DMA-1
4°
3°
2°
Cell Body
1° Dendrite
1°
Microtubule
-
+
RAB-3
SV
Axon
B
L4 Larva
PVD Neuron
mKate2::RAB-3
Control DEG
KNL-1 DEG
1° Dendrite
CB
Axon
C
RAB-3 Signal in Dendrite vs Axon
Axon
Dendrite
ns
ns
Mean Fluorescence (a.u.)
400
300
200
100
0
Control DEG (n=24)
KNL-1 DEG (n=23)
D
Anterior 1° Dendrite
1° Dendrite
CB
EB1EBP-2::GFP
Distal
Cell Body
Control DEG
KNL-1 DEG
Time
E
Retrograde
Anterograde
ns
ns
EBP-2 Comets (%)
100
50
0
Control DEG (n=13)
KNL-1 DEG (n=11)
F
Split-GFP System (PVD Tubulin)
PVD prom
Endogenous Locus
PVD Specific GFP::TBA-1
β1-10
β11
TBA-1
GFP::TBA-1
Anterior dendrite
ROI
CB
Control (n=33)
KNL-1 Degron (n=42)
Fluorescence Recovery (%)
30
20
10
0
Time (s)
0
20
40
60
80
100
120

Figure 4. PVD neuronal polarity & microtubule organization are not affected by post-mitotic degradation of KNL-1.

(A) Schematic showing DMA-1, the dendrite specific receptor, RAB-3, the synaptic vesicle (SV) marker & the anterior dendrite microtubule organization. **(B)** Localization of the synaptic marker RAB-3 in control & KNL-1 DEG. RAB-3 is enriched in the axon (see red arrowheads). Scale bar, 5µm. **(C)** Quantification of RAB-3 fluorescent signal in the dendrite & axon. **(D)** $EB1^{EBP-2}$::GFP dynamics in the anterior primary dendrite. Plus end comets (arrowhead) are highlighted in the top still image. Below are kymographs projection images of the control (top) & KNL-1 DEG. The kymograph was generated along line extending from cell body towards the distal end of the primary dendrite. Scale bar, 5µm. **(E)** Quantification of $EB1^{EBP-2}$::GFP comet dynamics in control & KNL-1 DEG. **(F)** (Top) Schematic of an endogenous GFP::TBA-1 fusion expressed specifically in PVD using a split-gfp system. (middle) Still image of the anterior primary dendrite that expresses the split-GFP::TBA-1. The red rectangle indicates the Region of Interest (ROI) that was bleached in the FRAP experiments. CB is cell body. Scale bar, 5µm (Bottom) GFP::TBA-1 fluorescence recovery plots for control & KNL-1 DEG.

Figure 5

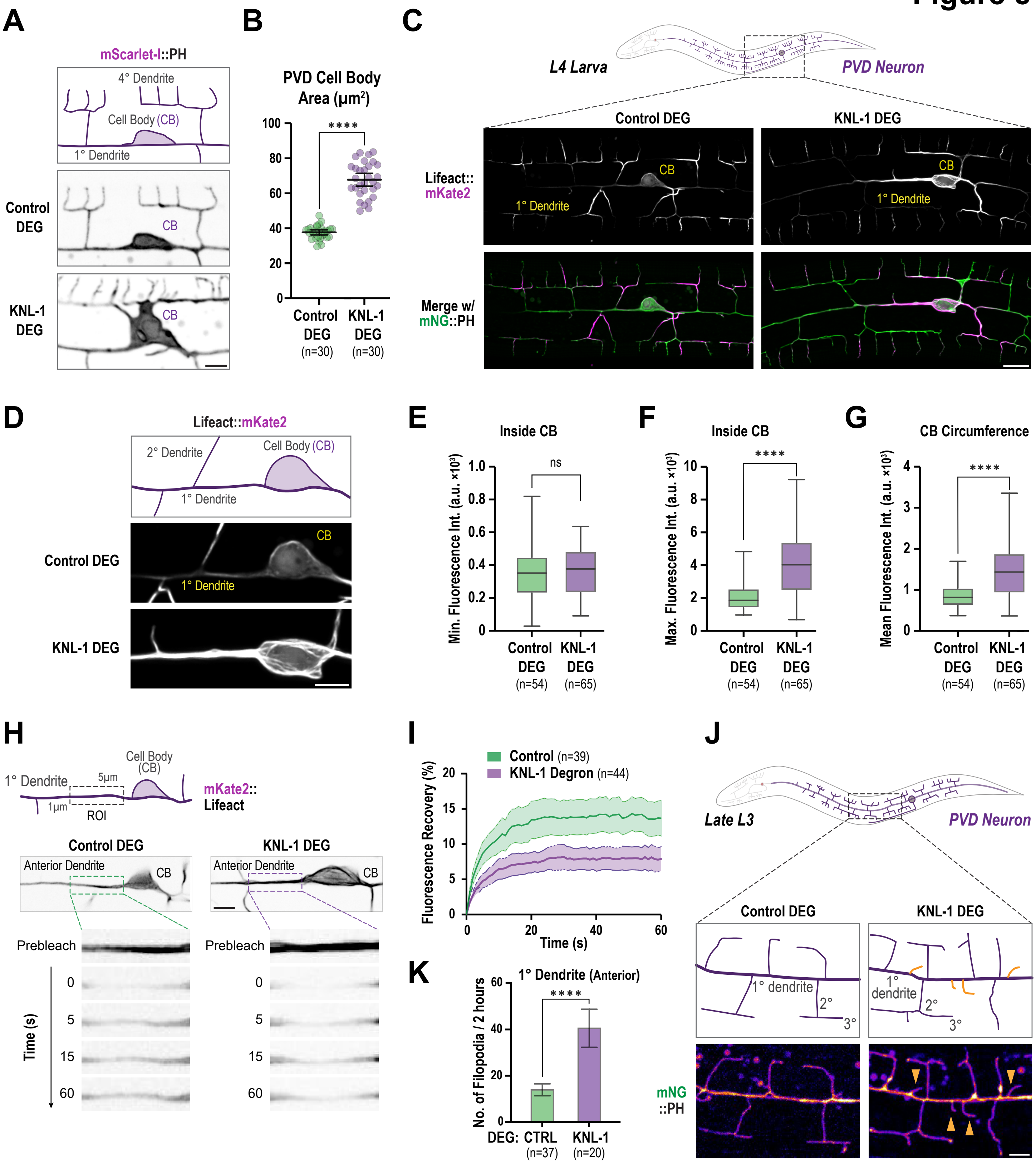
A
mScarlet-I::PH
4° Dendrite
Cell Body (CB)
1° Dendrite
Control DEG
CB
KNL-1 DEG
CB
B
PVD Cell Body Area (μm²)
****
Control DEG (n=30)
KNL-1 DEG (n=30)
C
L4 Larva
PVD Neuron
Control DEG
KNL-1 DEG
Lifeact:: mKate2
CB
1° Dendrite
Merge w/ mNG::PH
D
Lifeact::mKate2
2° Dendrite
Cell Body (CB)
1° Dendrite
Control DEG
KNL-1 DEG
E
Inside CB
ns
Min. Fluorescence Int. (a.u. ×10³)
Control DEG (n=54)
KNL-1 DEG (n=65)
F
Inside CB
****
Max. Fluorescence Int. (a.u. ×10³)
G
CB Circumference
Mean Fluorescence Int. (a.u. ×10³)
H
1° Dendrite
5μm
1μm
ROI
Cell Body (CB)
mKate2:: Lifeact
Anterior Dendrite
Prebleach
Time (s)
I
Control (n=39)
KNL-1 Degron (n=44)
Fluorescence Recovery (%)
Time (s)
J
Late L3
PVD Neuron
1° dendrite
2°
3°
mNG ::PH
K
1° Dendrite (Anterior)
No. of Filopodia / 2 hours
DEG: CTRL (n=37)
KNL-1 (n=20)

Figure 5. The PVD cell body shows an increase in polymerized actin after KNL-1 degradation.

(A) Images of the PVD cell body and proximal regions in control and KNL-DEG. Scale bar, 5µm. **(B)** Quantification of the area of the cell body in control & KNL-1 DEG animals. **(C)** The top image shows actin labeled with mKate2::Lifeact while the bottom shows actin overlaid with membrane (mNeonGreen::PH) in control & KNL-1 DEG animals. Scale bar, 10µm. **(D)** Images highlighting actin distribution in the cell body (CB) and proximal anterior primary dendrite in control (top) and KNL-1 DEG (bottom) animals. Scale bar, 5 µm. **(E-G)** Quantification of Lifeact fluorescence intensity inside and on the periphery of the cell body. **(H)** (Top) Still images of the PVD anterior primary dendrite expressing mKate2::Lifeact in control & KNL-1 DEG animals The dashed rectangles indicate the Region of Interests (ROIs) that were bleached in the FRAP experiments. (Bottom) Prebleach and postbleach images of mKate2::Lifeact in control & KNL-1 DEG animals. Scale bar, 5µm. **(I)** mKate2::Lifeact fluorescence recovery plots for control & KNL-1 DEG animals. **(J)** Images of anterior primary dendrite labeled with mNeonGreen::PH in control & KNL-1 DEG late L3 stage animals. Yellow arrowheads indicate filopodia. Scale bar, 5µm. **(K)** Quantification of the filopodial protrusions from anterior primary dendrite during a two-hour time lapse.

Figure 6

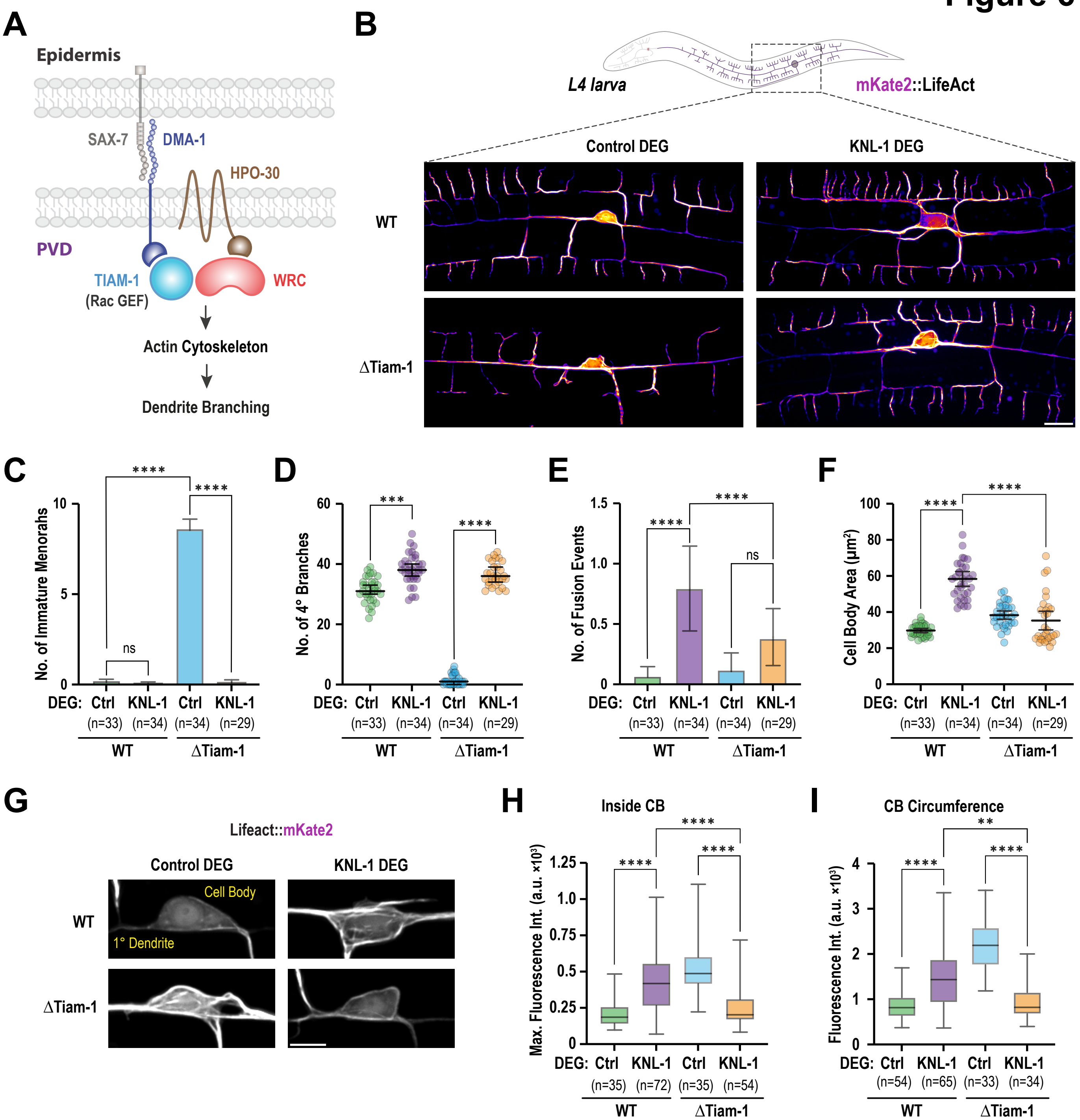
A
Epidermis
SAX-7
DMA-1
HPO-30
PVD
TIAM-1
(Rac GEF)
WRC
Actin Cytoskeleton
Dendrite Branching
B
L4 larva
mKate2::LifeAct
Control DEG
KNL-1 DEG
WT
ΔTiam-1
C
No. of Immature Menorahs
D
No. of 4° Branches
E
No. of Fusion Events
F
Cell Body Area (μm²)
DEG: Ctrl KNL-1 Ctrl KNL-1
(n=33) (n=34) (n=34) (n=29)
WT
ΔTiam-1
ns
G
Lifeact::mKate2
Control DEG
KNL-1 DEG
Cell Body
1° Dendrite
H
Inside CB
Max. Fluorescence Int. (a.u. ×10³)
DEG: Ctrl KNL-1 Ctrl KNL-1
(n=35) (n=72) (n=35) (n=54)
I
CB Circumference
Fluorescence Int. (a.u. ×10³)
(n=54) (n=65) (n=33) (n=34)

Figure 6. Degradation of KNL-1 rescues the dendrite branching defects in TIAM-1/RacGEF deletion animals.

(A) Schematic showing the signaling pathway involved in 3° & 4° dendrite branching. Interactions between the ligand SAX-7 expressed in epidermis and DMA-1 receptor in PVD recruits the TIAM-1/RacGEF which then promotes dendrite branching by activating actin polymerization. **(B)** Images of PVD dendrites expressing mKate2::Lifeact in indicated conditions. Scale bar, 10μm. **(C-E)** Quantification of PVD menorah organization in the indicated conditions. Menorahs that lack 4° branches are considered “immature menorahs”. **(F)** Quantification of the area of the cell body in the indicated conditions. **(G)** Images highlight actin distribution in the cell body and proximal anterior primary dendrite in indicated conditions. Scale bar, 5μm. **(H&I)** Quantification of Lifeact fluorescence intensity inside the cell body (CB) in the indicated conditions.

Figure S1

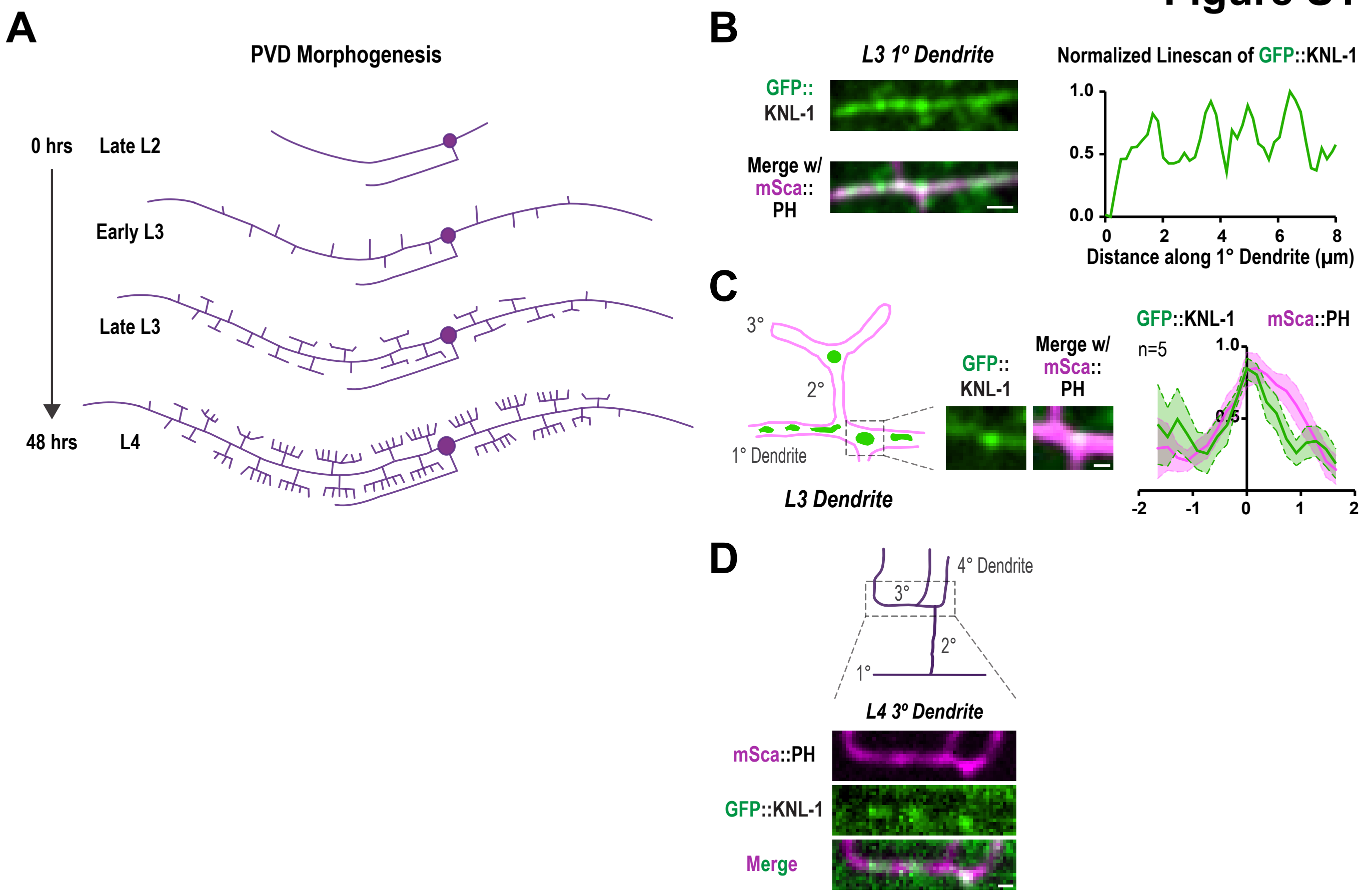
A
PVD Morphogenesis
0 hrs
Late L2
Early L3
Late L3
48 hrs
L4
B
L3 1º Dendrite
GFP::
KNL-1
Merge w/
mSca::
PH
Normalized Linescan of GFP::KNL-1
1.0
0.5
0.0
0
2
4
6
8
Distance along 1° Dendrite (µm)
C
3°
2°
1° Dendrite
L3 Dendrite
GFP::
KNL-1
Merge w/
mSca::
PH
GFP::KNL-1
mSca::PH
n=5
1.0
0.5
-2
-1
0
1
2
D
4° Dendrite
3°
2°
1°
L4 3º Dendrite
mSca::PH
GFP::KNL-1
Merge

Figure S1. PVD morphogenesis & KNL-1 localization.

(A) Schematic of the PVD neuron morphogenesis from L2 stage until the L4 larval stage. Dendrite outgrowth, branching and menorah formation takes about 48 hours. **(B)** (Left) Localization of GFP::KNL-1 within the primary dendrite at the L3 stage. KNL-1 forms distinct puncta like structures. Scale bar, 2 µm. (Right) Linescan of the GFP::KNL-1 intensity. The peaks correspond to the puncta seen on the image. **(C)** (Left) Schematic and image showing GFP::KNL-1 enrichment at the base of branchpoint between 1° and 2° dendrite at the L3 stage. Scale bar, 1 µm. (Right) Plot showing the average of the fluorescent intensity linescans of GFP::KNL-1 superimposed with that of mScarlet-I::PH. Branchpoints show an increased intensity of PH and KNL-1 signal. **(D)** Image shows distribution of GFP::KNL-1 within the 3° dendrite at the early L4 stage. Scale bar, 2 µm.

Figure S2

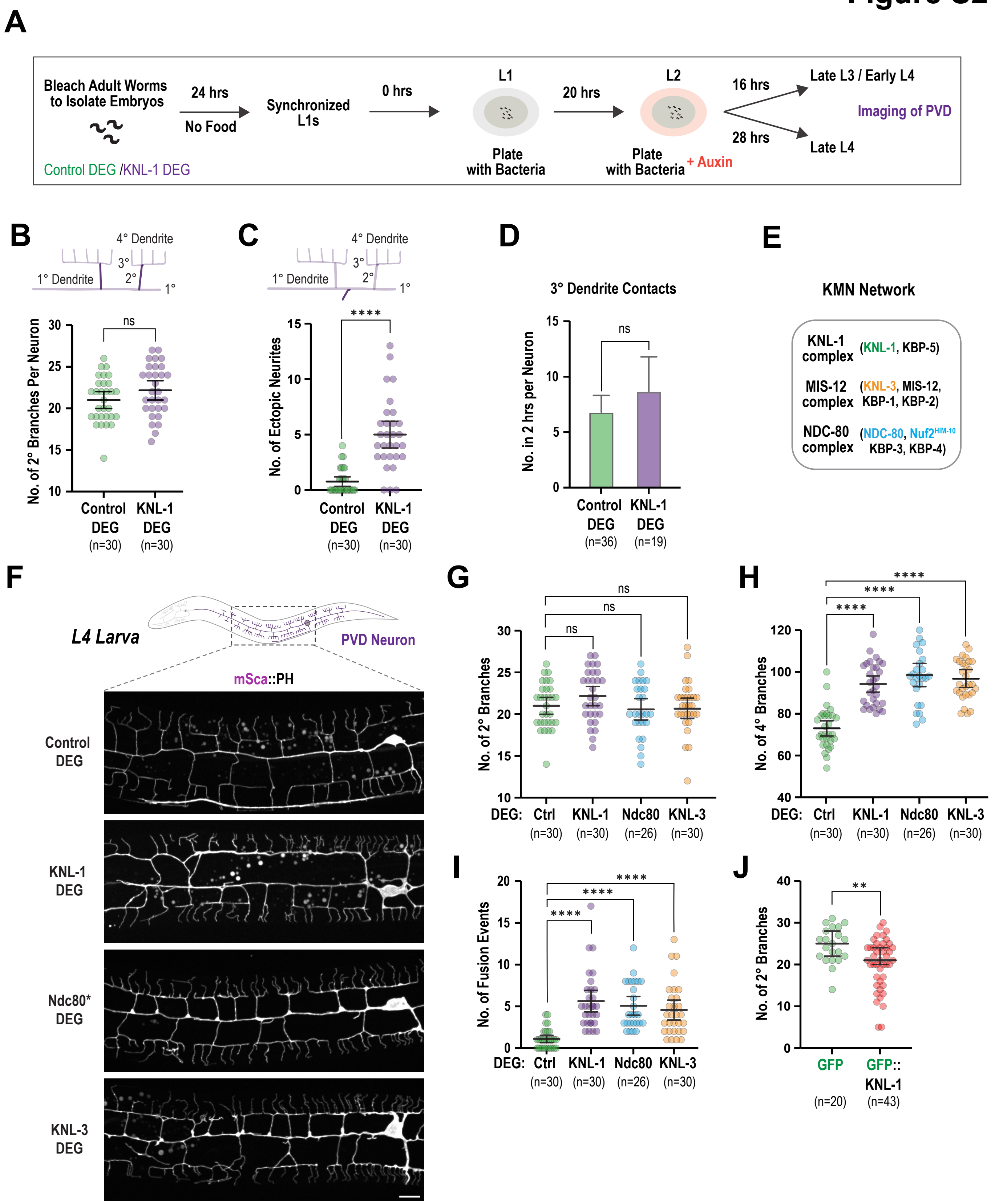
A
Bleach Adult Worms to Isolate Embryos
24 hrs
No Food
Synchronized L1s
0 hrs
L1
Plate with Bacteria
20 hrs
L2
Plate with Bacteria
+ Auxin
16 hrs
28 hrs
Late L3 / Early L4
Late L4
Imaging of PVD
Control DEG /KNL-1 DEG
B
4° Dendrite
3°
2°
1° Dendrite
1°
No. of 2° Branches Per Neuron
ns
Control DEG (n=30)
KNL-1 DEG (n=30)
C
No. of Ectopic Neurites
****
Control DEG (n=30)
KNL-1 DEG (n=30)
D
3° Dendrite Contacts
No. in 2 hrs per Neuron
ns
Control DEG (n=36)
KNL-1 DEG (n=19)
E
KMN Network
KNL-1 complex (KNL-1, KBP-5)
MIS-12 complex (KNL-3, MIS-12, KBP-1, KBP-2)
NDC-80 complex (NDC-80, Nuf2HIM-10 KBP-3, KBP-4)
F
L4 Larva
PVD Neuron
mSca::PH
Control DEG
KNL-1 DEG
Ndc80* DEG
KNL-3 DEG
G
No. of 2° Branches
ns
ns
ns
DEG: Ctrl (n=30) KNL-1 (n=30) Ndc80 (n=26) KNL-3 (n=30)
H
No. of 4° Branches
****
****
****
DEG: Ctrl (n=30) KNL-1 (n=30) Ndc80 (n=26) KNL-3 (n=30)
I
No. of Fusion Events
****
****
****
DEG: Ctrl (n=30) KNL-1 (n=30) Ndc80 (n=26) KNL-3 (n=30)
J
No. of 2° Branches
**
GFP (n=20)
GFP::KNL-1 (n=43)

Figure S2. Effects of degradation of KMN network on PVD morphology.

(A) Schematic indicates the experimental design for degrading AID::KNL-1. To obtain synchronized L1 animals, embryos from control or AID::KNL-1 adult worms expressing PVD-specific TIR1 transgene were isolated by bleach treatment and hatched for 24 hours on plates without food. L1 larvae were placed on a plate with food until they reached the L2 stage (20hrs). The L2 stage animals were transferred to plates with bacteria and auxin and grown until they reached L4 stage (24hrs). The late L4 stage animals have fully developed menorahs and were imaged to analyze the PVD morphology. **(B&C)** Quantification of the numbers of 2° branches and the number of ectopic branches in control & KNL-1 DEG. **(D)** Quantification of the filopodial protrusions from the anterior primary dendrite during two-hour time lapses. **(E)** Schematic of the components of the KNL1/Mis12/Ndc80 complex. **(F)** Images of PVD dendrite organization in control, KNL-1 DEG, Ndc80 DEG & KNL-3 DEG.* In the Ndc80 DEG, AID was fused to both NDC-80 & $NUF2^{Him1\text{-}10}$ subunits. Scale bar, 10 µm. **(G-I)** Quantification of PVD dendrite organization including the number of 2° & 4° branches and fusions between menorahs in the indicated conditions. **(J)** Quantification of the number of 2° branches in the dendrites of PVD in control and KNL-1::GFP overexpressing animals.

Figure S3

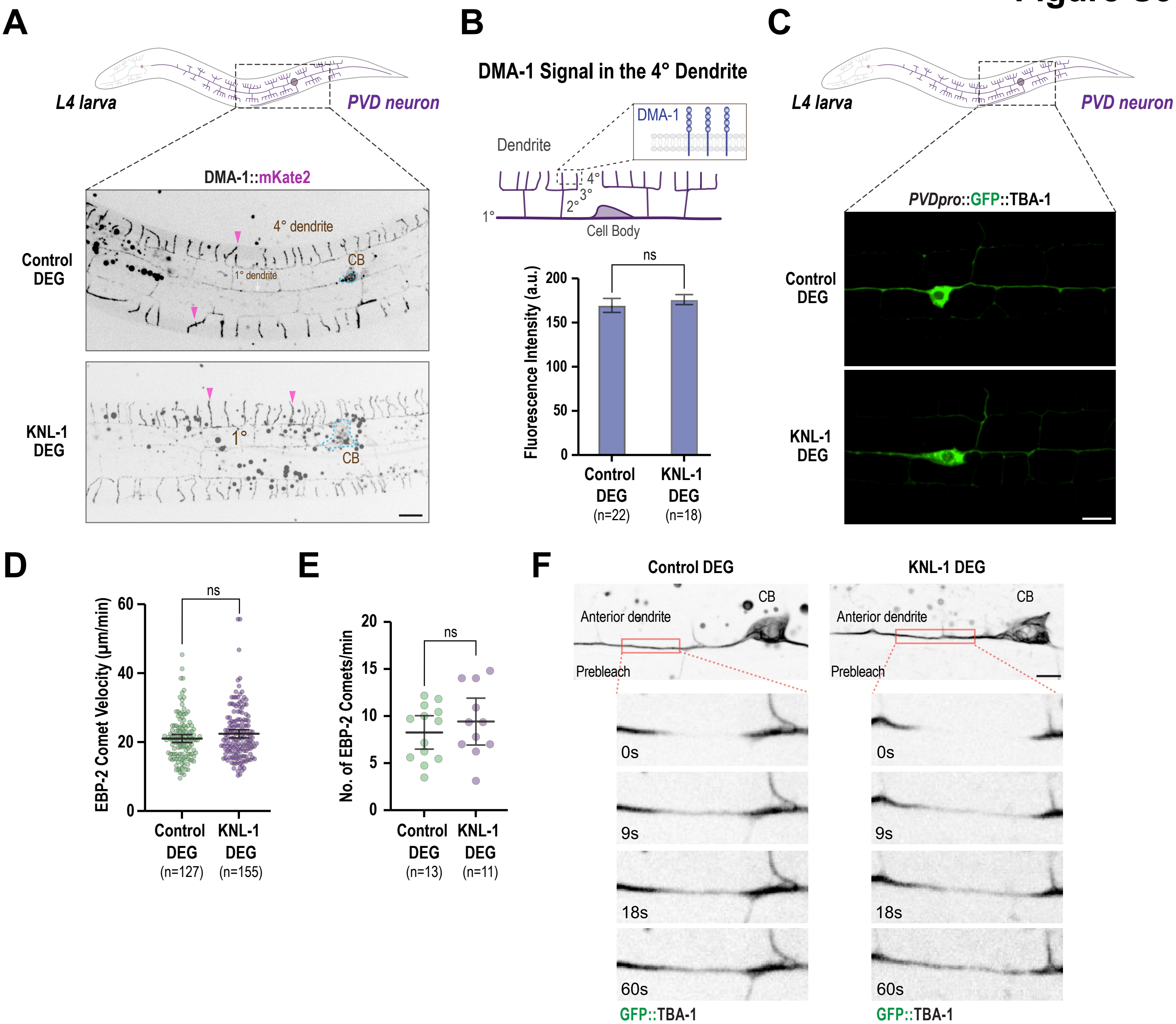
A
L4 larva
PVD neuron
DMA-1::mKate2
Control DEG
4° dendrite
1° dendrite
CB
KNL-1 DEG
1°
CB
B
DMA-1 Signal in the 4° Dendrite
DMA-1
Dendrite
4°
3°
2°
1°
Cell Body
ns
Fluorescence Intensity (a.u.)
Control DEG (n=22)
KNL-1 DEG (n=18)
C
L4 larva
PVD neuron
PVDpro::GFP::TBA-1
Control DEG
KNL-1 DEG
D
EBP-2 Comet Velocity (µm/min)
ns
Control DEG (n=127)
KNL-1 DEG (n=155)
E
No. of EBP-2 Comets/min
ns
Control DEG (n=13)
KNL-1 DEG (n=11)
F
Control DEG
KNL-1 DEG
Anterior dendrite
CB
Prebleach
0s
9s
18s
60s
GFP::TBA-1

Figure S3. DMA-1 distribution & microtubule organization & stability after degradation of KNL-1 in the PVD.

(A) Localization of the dendrite guidance receptor, DMA-1 in control & KNL-1 DEG at the L4 stage. Pink arrow heads show enrichment of DMA-1 in the 4° dendrite. Scale bar, 10μm. DMA-1 is restricted to dendrite structures and no axonal signal for DMA-1 is visible **(B)** Quantification of DMA-1 fluorescent signal in the PVD dendrites shows that both the control and KNL-1 has similar levels of DMA-1. **(C)** Images of Pdes-2 driven GFP::TBA-1 in the control & KNL-1 degrader animals. Tubulin distribution looks similar in both conditions. GFP::TBA-1 is detected predominantly in the 1° dendrite and is largely absent from the dendrite branches. Scale bar, 10 μm. **(D&E)** Quantification of $EB1^{EBP-2}$::GFP comet dynamics in control & KNL-1 DEG. **(F)** (Top) Still images of the PVD anterior primary dendrite expressing endogenous GFP::TBA-1 in control & KNL-1 DEG animals. Scale bar, 5 μm. The dashed rectangles indicate the Region of Interest (ROI) that were bleached in the FRAP experiments. (Bottom) Prebleach and postbleach images of GFP::TBA-1 in control & KNL-1 DEG animals.

Figure S4

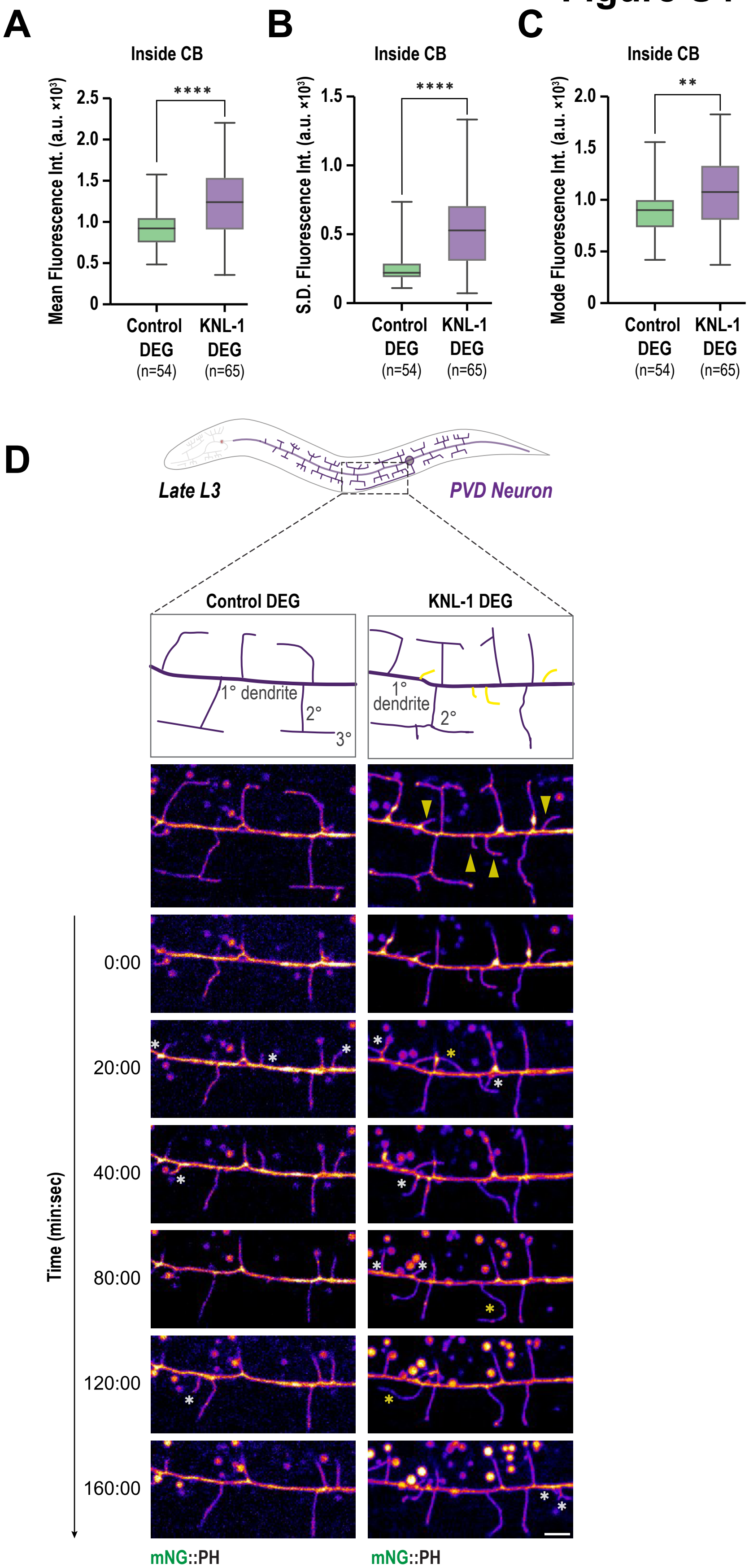
A
B
C
Inside CB
Mean Fluorescence Int. (a.u. ×10³)
S.D. Fluorescence Int. (a.u. ×10³)
Mode Fluorescence Int. (a.u. ×10³)
****
**
Control DEG (n=54)
KNL-1 DEG (n=65)
D
Late L3
PVD Neuron
Control DEG
KNL-1 DEG
1° dendrite
2°
3°
Time (min:sec)
0:00
20:00
40:00
80:00
120:00
160:00
mNG::PH

Figure S4. Analysis of F-actin distribution of in the control and KNL-1 degraded animals; filopodia dynamics in L3 animals.

(A-C) Quantification of Lifeact fluorescence intensity inside the cell body. **(D)** Snapshots of time lapse imaging of 1° dendrite branch dynamics in control & KNL-1 DEG animals at the late L3 stage. Yellow arrowheads indicate filopodia. White asterisks indicate newly formed filopodia. Yellow asterisks indicate the misguided filopodia that runs parallel to the 1° dendrite. Scale bar, 5 µm

Figure S5

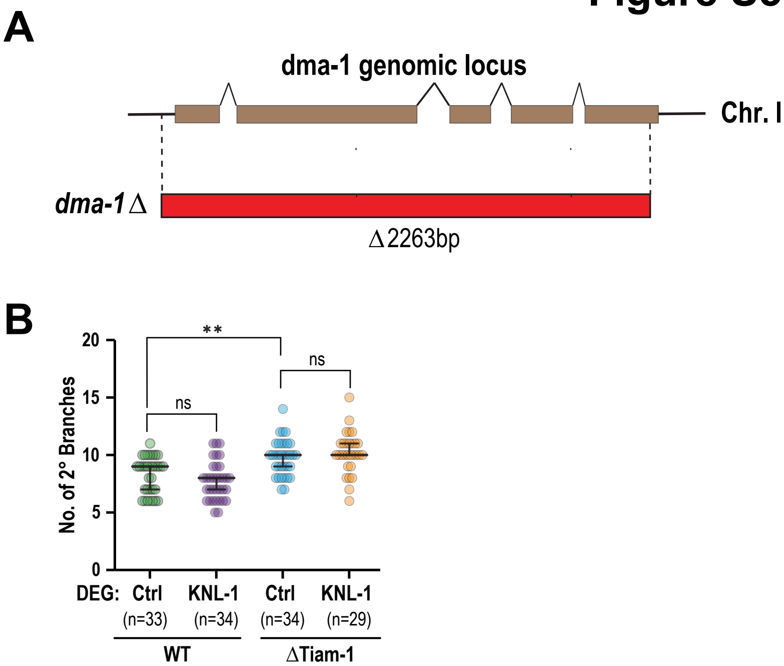
A
dma-1 genomic locus
Chr. I
dma-1 Δ
Δ2263bp
B
No. of 2° Branches
20
15
10
5
0
**
ns
ns
DEG: Ctrl
KNL-1
Ctrl
KNL-1
(n=33)
(n=34)
(n=34)
(n=29)
WT
ΔTiam-1

Figure S5. Analysis of KNL-1 degradation in dma-1 and tiam-1 deletion background.

(A) Schematic of the dma-1 gene deletion. Dashed line point to the location of the crRNAs that were used to generate the gene deletion. **(B)** Quantification of PVD 2° branches in the indicated conditions. tiam-1Δ shows a slight increase in the number of 2° branches. As the counts are from a single timepoint it is not clear whether these are stable 2° branches or long unstable filopodia.

MATERIALS AND METHODS

<u>*C. elegans* Strains & Methods</u>

All *C. elegans* strains were maintained at 20°C on standard Nematode Growth Media (NGM) plates seeded with OP50 bacteria. The genotypes of the *C. elegans* strains used in this study are described in *Table S1*.

Single copy transgenic integrations were engineered using the transposon based mos1 mediated Single Copy Insertion (mosSCI) method[40]. Briefly, the strains were generated by injecting a mixture of repair plasmid containing the transgene and a positive selection marker, transposase plasmid, and the three plasmids encoding fluorescent markers for negative selection [pCFJ90 (P*myo-2::mCherry*), pCFJ104 (P*myo-3::mCherry*) and pGH8 (P*rab-3::mCherry*)] into appropriate *C. elegans* strains that contain mos1 insertion sites at specific genomic locations within Chr I, II, IV or V. Positive integrants were identified by selecting worms that were moving and did not contain fluorescent selection markers. Integration of transgenes were confirmed by PCR, spanning both homology arms. Endogenous tagging of various genes (see *Table S1*) at the N- or C-teminus and generation of the *dma-1* deletion were done using CRISPR/Cas9 methods [41–43]. The specific method and guide RNAs used to generate each strain are described in *Table S2*. Briefly, a DNA mix (Dickinson et al., 2015; Waaijers et al., 2013) or Cas9RNP mix (Paix et al., 2015), containing the respective repair template, guide RNA sequences, Cas9 and selection markers were injected into N2 animals. Recombinant strains were identified by appropriate selection method and were confirmed by PCR, spanning both homology regions. All plasmids used for the strain constructions were constructed using the Gibson Assembly method [44].

Auxin Degradation

Worms were synchronized at L1 arrest stage by bleaching gravid adults in NGM plate using a 1M sodium hydroxide and 2.5% sodium hypochlorite (Acros Organics) solution to obtain eggs. The eggs were then left to hatch for 48 hours at 20°C allow hatched L1 larvae to enter L1 arrest stage. Subsequently, the worms were washed with M9 buffer and transferred into a centrifuge tube for pelleting for 1 min at 1000 RPM. The pelleted synchronized L1s were transferred to OP-50 seeded NGM plates and maintained at 20°C (T=0hr). Auxin treatment was performed by transferring worms to OP-50 seeded NGM plates containing 4 mM auxin (K-NAA, N160, Phytochrome laboratories) at T=20hr post synchronization. The auxin containing NGM plates were seeded with 200μl of high-density OP-50 and left to dry for 2 days at room temperature. The seeded plates were stored for up to 1 month at 4°C.

Fluorescence microscopy and image analysis

To image PVD neurons expressing the appropriate markers L2 or L4 stage worms were anaesthetized in 5 mM Levamisole and mounted in M9 on a 2% agarose pad. Images were acquired using a spinning disc confocal imaging system with a Yokogawa spinning disk unit (CSU-W1), a Nikon Ti2-E fully motorized inverted microscope, with a CFI60 Plan Apochromat lambda 60X Oil (Nikon) objective and a Photometrics Prime 95B camera. For imaging Lifeact::mKate2 marker a CFI60 Plan Apochromat lambda 100X Oil (Nikon) objective was used. Z-stacks of 0.5 μm or 1.0 μm were acquired to cover the PVD closer to the side facing the coverslip / objective.

To quantify KNL-1 degradation the Z-stacks were projected into a maximum intensity projection. The mean intensity of KNL-1::GFP at the cell body was measured using a polygon selection drawn over the cell body boundary using Image J (Fiji).

To quantify co-localization of mSca::PH with KNL1::GFP separate line scans were acquire using a segmented line (width=1 pixels) at a maximum of 2 μm of either side of the branchpoint/base of the branch using Image J (Fiji). The values were normalized to the maximum and minimum intensity value.

To quantify the morphology of the PVD dendrites the Z-stacks were projected into a maximum intensity projection. The various dendrite morphology parameters were measured separately for the posterior dendrite and the anterior proximal dendrite (100μm & 50 μm from the soma for worms expressing the PH marker & Lifeact marker, respectively). The 2° dendrites were identified as orthogonal branches to 1°dendrite containing higher order branches (3° and/or 4° branches). The 4° dendrites were identified as orthogonal branches to the 3°dendrites. Fusion was identified as two adjacent 3° dendrite lacking a gap (Smith et al., 2012). Ectopic branches were identified as branches protruding out of the 1° dendrite with a length of at least 2x higher than its width and with no higher order branches. The cell body area was measured using a polygon selection drawn over the cell body boundary using Image J (Fiji).

To quantify the morphology of the PVD dendrites for the extrachromosomal arrays the fluorescence intensity of GFP or KNL-1::GFP were measured in the cell body using the polygon selection drawn over the cell body boundary using Image J (Fiji). The values were normalised to the background fluorescence intensity to ensure only worms with over-expression were included in the analysis. Hence, if the intensity was greater than half the max recorded intensity then the worms were included in the analysis. The morphology was quantified for the whole neuron using the parameters previously described.

To quantify RAB-3 signal the Z-stacks were projected into a maximum intensity projection and the fluorescence intensity was measured along the length of the axon of each neuron and along an equivalent length in the proximal anterior dendrite using a segmented line (width=3 pixels) in Image J (Fiji). To quantify DMA-1 signal the Z-stacks were projected into a maximum intensity projection and the fluorescence intensity was measured in the 4° dendrites adjacent to the cell body using a segmented line (width=3 pixels) in Image J (Fiji).

To quantify actin distribution at the cell body the Z-stacks were projected into a maximum intensity projection of the z-planes that included one single PVD neuron (~18 x 1 µm z-stacks). Mean intensity of actin around the cell body was measured using a segmented line (width=3 pixels) drawn over the cell body boundary with the anterior side as the start point and following a clockwise direction using Image J (Fiji). The standard deviation, maximum and minimum intensity of actin at the cell body were measured using a polygon selection drawn over the cell body boundary using Image J (Fiji).

To quantify membrane blebbing in L4 worms the Z-stacks were projected into a maximum intensity projection and membrane blebbing was quantified for the whole anterior dendrite.

To quantify LGG-1 puncta in day 3 adults, the Z-stacks were projected into a maximum intensity projection and a 50 µm x 50 µm section centred around the cell body was analysed for each worm. LGG-1 puncta were counted if they were not in the cell body or axon initial segment.

Timelapse Imaging

For time-lapse imaging of dendrite dynamics, synchronized worms were anesthetized in 5 mM Levamisole after auxin treatment at 8 hours post synchronization or in the absence of treatment. 9-11 x 0.9 µm z-stacks were acquired at 1 frame per 1:20 minutes for 2 hours and an exposure of 50 ms. Acquisition was performed using using a spinning disc confocal imaging system with a Yokogawa spinning disk unit (CSU-W1), a Nikon Ti2-E fully motorized inverted microscope, with a CFI60 Plan Apochromat lambda 60X Oil (Nikon) objective and Photometrics Prime 95B camera.

For quantifications, time of contact of 3^{o} dendrites, number of contacts and number of unresolved of contacts were measured from maximum intensity projections of z-stacks using Image J (Fiji). This quantification was performed for the first 100 µm anterior to the soma. Contacts of 3^{o} dendrites were identified as two adjacent 3^{o} dendrite lacking a gap (Smith et al., 2012). Only the contacts that occurred during the timelapse acquisition were quantified. Unresolved contacts were identified as contacts that lacked a gap by the end of the timelapses. Protrusions were identified as any membrane protrusions smaller than 2.5 µm.

For timelapse imaging of EBP-2 dynamics synchronized worms were anesthetized in 5 mM Levamisole after auxin treatment. A single z-slice was acquired of the first 50 µm of the anterior dendrite at 1 frame per 1 sec using a spinning disc confocal imaging system with a Yokogawa spinning disk unit (CSU-W1), a Nikon Ti2-E fully motorized inverted microscope, with a CFI60 Plan Apochromat lambda 100X Oil (Nikon) objective and an Photometrics Prime 95B camera. For the generation of kymographs Fiji plugin, KymographClear 2.0a[45] was used. A line of width 2 pixel was drawn to generate kymograph. The number of lines (indicative of the number of comets) in each direction was measured and the length and height of each line was used to calculate the velocities of each individual comet.

Fluorescence Recovery After Photobleaching (FRAP) of Actin and Microtubule

For FRAP imaging of microtubule marker worms were anesthetized in 5 mM Levamisole. A single z-slice was acquired of the first 50 µm of the anterior dendrite at 1 frame per 1 sec. After 3 prebleach frames, 1.5 µm region 20 µm away from the cell body was bleached using 405 nm laser at 30% power, 150 µs dwell time and 5 laser iterations. Images were acquired for 2 minutes post bleaching. For FRAP imaging of actin marker worms were anesthetized in 5 µl 5mM Levamisole in M9. A single z-slice was acquired of the first 50 µm of the anterior dendrite at 1 frame per 1 sec and an exposure of 150 ms. After 3 prebleach frames, 1.5 µm region 20 µm away from the cell body was bleached using 405 nm laser at 40% power, 300 µs. Dwell time and 5 laser iterations. Images were acquired for 2 minutes post bleaching.

To quantify fluorescence intensity a region of interest (ROI) of 1.5 µm was defined using elliptical selection in Image J (Fiji). The fluorescence intensity was normalized to the background and corrected for the fluorescence intensity of non-bleached area. Additionally, the FRAP actin marker analysis required the values to be additionally subtracted by the intensity at the photobleached region 1 frame post photobleaching.

Behavioural assays

For the locomotion assays L4 worms were transferred to a freshly seeded NGM plate for 1 hour at 20^{o}C after auxin treatment. Acquisition was performed using Nikon SMZ18 microscope at 2X P2-SHR Plan Apo 1X objective and Photometrics Cool SNAP camera. 5 tracks were measured per worm and 15 worms were measured per strain. The wavelength was measured as the distance between two successive peaks and the amplitude as half the measurement of the height between two opposing peaks. Five measurements were taken per track.

Quantification and Statistical Analysis

Details of the methods employed to extract and quantify various parameters in microscopy datasets are described in the image analysis section. The statistical tests used to determine significance are described in the figure legends. The data normality was assessed using a Shapiro-Wilk test. For normally distributed data either an unpaired t-test (for comparisons between two groups) or an ordinary one-way ANOVA with a follow up Holm-Sidak multiple comparison test (for comparisons between three and more groups) were performed. For data sets that did not pass the normality test either a Mann-Whitney test (for comparisons between two groups) or a Kruskal-Wallis test with a follow up Dunn's multiple comparison test (for comparisons between three and more groups) were performed. All comparisons were done in GraphPad Prism (GraphPad Software) and the stars ****, ***, ** and ns correspond $p<0.0001$, $p<0.001$, $p<0.01$ and "not significant", respectively.

Table S1. *C. elegans* Strains

STRAIN DESCRIPTION	SOURCE	IDENTIFIER
dhaSI145 [oxTi185; pDC973; Pdes-2--TIR1--F2A--mTagBFP--AID--NLS--tbb-23'UTR; cb-unc-119(+)]I #1; dhaSi89 [pDC747; Punc-86::TIR-1::unc543'UTR; cb-unc-119(+)]II #1; ; unc-119(ed3)III?; dhaSi76[oxTi177;PDC731; Pdes-2::mSca-PH::unc-54 3'UTR; cb-unc-119(+)] IV*	This study	DKC815
dhaSI145 [oxTi185; pDC973; Pdes-2--TIR1--F2A--mTagBFP--AID--NLS--tbb-23'UTR; cb-unc-119(+)]I #1; dhaSi89 [pDC747; Punc-86::TIR-1::unc543'UTR; cb-unc-119(+)]II #1; knl-1(dha122 (AID::dTagmB>F>P::::KNL-1))III ; unc-119(ed3)III?; dhaSi76[oxTi177;PDC731; Pdes-2::mSca-PH::unc-54 3'UTR; cb-unc-119(+)] IV*	This study	DKC849
dhaSI145 [oxTi185; pDC973; Pdes-2--TIR1--F2A--mTagBFP--AID--NLS--tbb-23'UTR; cb-unc-119(+)]I #1; dhaSi89 [pDC747; Punc-86::TIR-1::unc543'UTR; cb-unc-119(+)]II #1; ; dhaSi76[ndc-80(dha148; NDC-80::AID::dgfp^3XFLAG) ; oxTi177;PDC731; Pdes-2::mSca-PH::unc-54 3'UTR; cb-unc-119(+)] IV dhaSi76[oxTi177;PDC731; Pdes-2::mSca-PH::unc-54 3'UTR; cb-unc-119(+)] IV*	This study	DKC860
dhaSI145 [oxTi185; pDC973; Pdes-2--TIR1--F2A--mTagBFP--AID--NLS--tbb-23'UTR; cb-unc-119(+)]I #1; dhaSi89 [pDC747; Punc-86::TIR-1::unc543'UTR; cb-unc-119(+)]II #1; unc-119(ed3)III?; dhaSi76[oxTi177;PDC731; Pdes-2::mSca-PH::unc-54 3'UTR; cb-unc-119(+)] IV; KNL-3(du2 [AID::KNL-3]) V*	This study	DKC911
dhaEx1[Pdes-2::Knl-1::GFP::unc 54 3'UTR]; dhaSi76[oxTi177;PDC731; Pdes-2::mSca-PH::unc-54 3'UTR; cb-unc-119(+)] IV	This study	DKC822
dhaEx3[Pdes-2::GFP::unc 54 3'UTR]; dhaSi76[oxTi177;PDC731; Pdes-2::mSca-PH::unc-54 3'UTR; cb-unc-119(+)] IV	This study	DKC824
dhaSI145 [oxTi185; pDC973; Pdes-2--TIR1--F2A--mTagBFP--AID--NLS--tbb-23'UTR; cb-unc-119(+)]I #1; dhaSi89 [pDC747; Punc-86::TIR-1::unc543'UTR; cb-unc-119(+)]II #1; knl-1(dha122 (AID::dTagmB>F>P::::KNL-1))III ; unc-119(ed3)III?; hrtSi17[Pdes-2::mKate2::rab-3 LG]IV*	This study	DKC1002
dhaSI145 [oxTi185; pDC973; Pdes-2--TIR1--F2A--mTagBFP--AID--NLS--tbb-23'UTR; cb-unc-119(+)]I #1; dhaSi89 [pDC747; Punc-86::TIR-1::unc543'UTR; cb-unc-119(+)]II #1; unc-119(ed3)III?; hrtSi17[Pdes-2::mKate2::rab-3 LG]IV*	This study	DKC1001
dhaSI145 [oxTi185; pDC973; Pdes-2--TIR1--F2A--mTagBFP--AID--NLS--tbb-23'UTR; cb-unc-119(+)]I #1; dhaSi89 [pDC747; Punc-86::TIR-1::unc543'UTR; cb-unc-119(+)]II #1; dhaSi272[oxTi177; pDC1122 ;Pser2-prom-3::DMA-1::mKate2::unc 54 3'UTR ; cb-unc-119(+)]V*	This study	DKC1076
dhaSI145 [oxTi185; pDC973; Pdes-2--TIR1--F2A--mTagBFP--AID--NLS--tbb-23'UTR; cb-unc-119(+)]I #1; dhaSi89 [pDC747; Punc-86::TIR-1::unc543'UTR; cb-unc-119(+)]II #1; knl-1(dha122 (AID::dTagmB>F>P::::KNL-1))III ; unc-119(ed3)III?; dhaSi272[oxTi177; pDC1122 ;Pser2-prom-3::DMA-1::mKate2::unc 54 3'UTR ; cb-unc-119(+)]V*	This study	DKC1075
dhaSI145 [oxTi185; pDC973; Pdes-2--TIR1--F2A--mTagBFP--AID--NLS--tbb-23'UTR; cb-unc-119(+)]I #1; dhaSi89 [pDC747; Punc-86::TIR-1::unc543'UTR; cb-unc-119(+)]II #1; dhaSi76[oxTi177;PDC731; Pdes-2::mSca-PH::unc-54 3'UTR; cb-unc-119(+)] IV; dhaSi241[oxTi177;PDC978; Pdes-2::GFP::tba-1::unc-54-3'UTR; cb-unc-119(+)] V #1*	This study	DKC917

dhaSI145 [oxTi185; pDC973; Pdes-2--TIR1--F2A--mTagBFP--AID--NLS--tbb-23'UTR; cb-unc-119(+)]I #1; dhaSi89 [pDC747; Punc-86::TIR-1::unc543'UTR; cb-unc-119(+)]II #1; knl-1(dha122 (AID::dTagmB>F>P::::KNL-1))III ; unc-119(ed3)III?; dhaSi76[oxTi177;PDC731; Pdes-2::mSca-PH::unc-54 3'UTR; cb-unc-119(+)] IV; dhaSi241[oxTi177;PDC978; Pdes-2::GFP::tba-1::unc-54-3'UTR; cb-unc-119(+)] V #1*	This study	DKC916
dhaSI145 [oxTi185; pDC973; Pdes-2--TIR1--F2A--mTagBFP--AID--NLS--tbb-23'UTR; cb-unc-119(+)]I #1; dhaSi89 [pDC747; Punc-86::TIR-1::unc543'UTR; cb-unc-119(+)]II #1; knl-1(dha122 (AID::dTagmB>F>P::::KNL-1))III; dhaSi45[oxTi365; pDC675; Pdes-2::mNG-PH::unc-54 3'UTR; cb-unc-119(+)] V clone A*	This study	DKC1089
dhaSi89 [pDC747; Punc-86::TIR-1::unc543'UTR; cb-unc-119(+)]II #1; knl-1(dha130; HA::7XGFP11::knl-1)III; dhaSi76[oxTi177;PDC731; Pdes-2::mSca-PH::unc-54 3'UTR; cb-unc-119(+)] IV ;outcrossed 3X ; dhaSi207 [pDC1020;unc-86pro::splitGFP1-10::tbb-2 3'UTR; cb-unc-119(+)] V #2	This study	DKC1139
dhaSi89 [pDC747; Punc-86::TIR-1::unc543'UTR; cb-unc-119(+)]II #1; knl-1(dha185; HA::7XGFP11::knl-1::AID)III; dhaSi76[oxTi177;PDC731; Pdes-2::mSca-PH::unc-54 3'UTR; cb-unc-119(+)] IV ;outcrossed 3X ; dhaSi207 [pDC1020;unc-86pro::splitGFP1-10::tbb-2 3'UTR; cb-unc-119(+)] V	This study	DKC1151
dhaSi207 [pDC1020;unc-86pro::splitGFP1-10::tbb-2 3'UTR; cb-unc-119(+)] II #2; knl-1(dha130; HA::7XGFP11::knl-1)III unc-119(ed3)III; dhaSi76[oxTi177;PDC731; Pdes-2::mSca-PH::unc-54 3'UTR; cb-unc-119(+)] IV ;outcrossed 3X	This study	DKC870
dhaSi249 [oxTi177; pDC732 Punc-86::mSca-PH::unc-54 3'UTR] V #1; dhaSi207 [pDC1020;unc-86pro::splitGFP1-10::tbb-2 3'UTR; cb-unc-119(+)] II #2; knl-1(dha130; HA::7XGFP11::knl-1)III	This study	DKC872
dhaSI145 [oxTi185; pDC973; Pdes-2--TIR1--F2A--mTagBFP--AID--NLS--tbb-23'UTR; cb-unc-119(+)]I #1; dhaSi89 [pDC747; Punc-86::TIR-1::unc543'UTR; cb-unc-119(+)]II #1; dhaSi243[pDC929; oxTi365; Pdes-2--LifeAct-mKate2--tbb-2 3UTR; cb-unc-119(+)]IV #1*	This study	DKC1035
dhaSI145 [oxTi185; pDC973; Pdes-2--TIR1--F2A--mTagBFP--AID--NLS--tbb-23'UTR; cb-unc-119(+)]I #1; dhaSi89 [pDC747; Punc-86::TIR-1::unc543'UTR; cb-unc-119(+)]II #1; knl-1(dha122 (AID::dTagmB>F>P::::KNL-1))III ; unc-119(ed3)III?; dhaSi243[pDC929; oxTi365; Pdes-2--LifeAct-mKate2--tbb-2 3UTR; cb-unc-119(+)]IV #1*	This study	DKC1057
dhaSI145 [oxTi185; pDC973; Pdes-2--TIR1--F2A--mTagBFP--AID--NLS--tbb-23'UTR; cb-unc-119(+)]I #1; dhaSi89 [pDC747; Punc-86::TIR-1::unc543'UTR; cb-unc-119(+)]II #1; dhaSi243[pDC929; oxTi365; Pdes-2--LifeAct-mKate2--tbb-2 3UTR; cb-unc-119(+)]IV #1; dhaSi45[oxTi365; pDC675; Pdes-2::mNG-PH::unc-54 3'UTR; cb-unc-119(+)] V clone A*	This study	DKC1087
dhaSI145 [oxTi185; pDC973; Pdes-2--TIR1--F2A--mTagBFP--AID--NLS--tbb-23'UTR; cb-unc-119(+)]I #1; dhaSi89 [pDC747; Punc-86::TIR-1::unc543'UTR; cb-unc-119(+)]II #1; knl-1(dha122 (AID::dTagmB>F>P::::KNL-1))III ; unc-119(ed3)III?; dhaSi243[pDC929; oxTi365; Pdes-2--LifeAct-mKate2--tbb-2 3UTR; cb-unc-119(+)]IV #15; pDC675; Pdes-2::mNG-PH::unc-54 3'UTR; cb-unc-119(+)] V clone A*	This study	DKC1113
dhaSI145 [oxTi185; pDC973; Pdes-2--TIR1--F2A--mTagBFP--AID--NLS--tbb-23'UTR; cb-unc-119(+)]I #1;tiam-1(ok772) I; dhaSi89 [pDC747; Punc-86::TIR-1::unc543'UTR; cb-unc-119(+)]II #1; knl-1(dha122 (AID::dTagmB>F>P::::KNL-1))III ; unc-119(ed3)III?; dhaSi243[pDC929; oxTi365; Pdes-2--LifeAct-mKate2--tbb-2 3UTR; cb-unc-119(+)]IV #1*	This study	DKC1103
tiam-1(ok772) I; dhaSi89 [pDC747; Punc-86::TIR-1::unc543'UTR; cb-unc-119(+)]II #1; unc-119(ed3)III?; dhaSi243[pDC929; oxTi365; Pdes-2--LifeAct-mKate2--tbb-2 3UTR; cb-unc-119(+)]IV #1	This study	DKC1109

dma-1 (dha155; DEL)I; dhaSi89 [pDC747; Punc-86::TIR-1::unc543'UTR; cb-unc-119(+)]II #1; dhaSi243[pDC929; oxTi365; Pdes-2--LifeAct-mKate2--tbb-2 3UTR; cb-unc-119(+)]IV #1	This study	DKC1145
dma-1 (dha155; DEL)I; dhaSi89 [pDC747; Punc-86::TIR-1::unc543'UTR; cb-unc-119(+)]II #1; knl-1(dha122 (AID::dTagmB>F>P::::KNL-1))III; dhaSi243[pDC929; oxTi365; Pdes-2--LifeAct-mKate2--tbb-2 3UTR; cb-unc-119(+)]IV #1	This study	DKC1147
dhaSI145 [oxTi185; pDC973; Pdes-2--TIR1--F2A--mTagBFP--AID--NLS--tbb-23'UTR; cb-unc-119(+)]I #1; dha149(HA::GFP11::tba-1)I; dhaSi89 [pDC747; Punc-86::TIR-1::unc543'UTR; cb-unc-119(+)]II #1; ; unc-119(ed3)III?; dhaSi76[oxTi177;PDC731; Pdes-2::mSca-PH::unc-54 3'UTR; cb-unc-119(+)] IV; dhaSi207 [pDC1020;unc-86pro::splitGFP1-10::tbb-2 3'UTR; cb-unc-119(+)] V #2*	This study	DKC1086
dhaSI145 [oxTi185; pDC973; Pdes-2--TIR1--F2A--mTagBFP--AID--NLS--tbb-23'UTR; cb-unc-119(+)]I #1; dha149(HA::GFP11::tba-1)I; dhaSi89 [pDC747; Punc-86::TIR-1::unc543'UTR; cb-unc-119(+)]II #1; knl-1(dha122 (AID::dTagmB>F>P::::KNL-1))III; unc-119(ed3)III?; dhaSi76[oxTi177;PDC731; Pdes-2::mSca-PH::unc-54 3'UTR; cb-unc-119(+)] IV; dhaSi207 [pDC1020;unc-86pro::splitGFP1-10::tbb-2 3'UTR; cb-unc-119(+)] V #2*	This study	DKC1090
dhaSI145 [oxTi185; pDC973; Pdes-2--TIR1--F2A--mTagBFP--AID--NLS--tbb-23'UTR; cb-unc-119(+)]I #1; dhaSi89 [pDC747; Punc-86::TIR-1::unc543'UTR; cb-unc-119(+)]II #1; knl-1(dha122 (AID::dTagmB>F>P::::KNL-1))III ; unc-119(ed3)III?; dhaSi76[oxTi177;PDC731; Pdes-2::mSca-PH::unc-54 3'UTR; cb-unc-119(+)] IV; dhaSi269[oxTi177; pDC1106 ;Pser-2prom3::ebp-2::gfp::tbb-2 3'UTR ; cb-unc-119(+)]V #1*	This study	DKC1072
dhaSI145 [oxTi185; pDC973; Pdes-2--TIR1--F2A--mTagBFP--AID--NLS--tbb-23'UTR; cb-unc-119(+)]I #1; dhaSi89 [pDC747; Punc-86::TIR-1::unc543'UTR; cb-unc-119(+)]II #1; unc-119(ed3)III?; dhaSi76[oxTi177;PDC731; Pdes-2::mSca-PH::unc-54 3'UTR; cb-unc-119(+)] IV; dhaSi269[oxTi177; pDC1106 ;Pser-2prom3::ebp-2::gfp::tbb-2 3'UTR ; cb-unc-119(+)]V #1*	This study	DKC1073
dhaSI145 [oxTi185; pDC973; Pdes-2--TIR1--F2A--mTagBFP--AID--NLS--tbb-23'UTR; cb-unc-119(+)]I #1; dhaSi89 [pDC747; Punc-86::TIR-1::unc543'UTR; cb-unc-119(+)]II #1; unc-119(ed3)III?; dhaSi76[oxTi177;PDC731; dhaSi237[oxTi177; pDC1061;Pser-2prom3::mscarlet::linker::LGG1:unc 54 3'UTR; cb-unc-119(+)]V #1*	This study	DKC1127
dhaSI145 [oxTi185; pDC973; Pdes-2--TIR1--F2A--mTagBFP--AID--NLS--tbb-23'UTR; cb-unc-119(+)]I #1; dhaSi89 [pDC747; Punc-86::TIR-1::unc543'UTR; cb-unc-119(+)]II #1; knl-1(dha122 (AID::dTagmB>F>P::::KNL-1))III ; unc-119(ed3)III?; dhaSi76[oxTi177;PDC731;dhaSi237[oxTi177; pDC1061;Pser-2prom3::mscarlet::linker::LGG1:unc 54 3'UTR; cb-unc-119(+)]V #1*	This study	DKC1126
dhaSI145 [oxTi185; pDC973; Pdes-2--TIR1--F2A--mTagBFP--AID--NLS--tbb-23'UTR; cb-unc-119(+)]I #1; dhaSi89 [pDC747; Punc-86::TIR-1::unc543'UTR; cb-unc-119(+)]II #1; unc-119(ed3)III?; unc-119 (ed3)III; dhaSi53[oxTi177;pDC675; Pdes-2::Mng-PH::unc-54 3'UTR; cb-unc-119 (+)]IV clone B; dhaSi237[oxTi177; pDC1061;Pser-2prom3::mscarlet::linker::LGG1:unc 54 3'UTR; cb-unc-119(+)]V #1*	This study	DKC1132
dhaSI145 [oxTi185; pDC973; Pdes-2--TIR1--F2A--mTagBFP--AID--NLS--tbb-23'UTR; cb-unc-119(+)]I #1; dhaSi89 [pDC747; Punc-86::TIR-1::unc543'UTR; cb-unc-119(+)]II #1; knl-1(dha122 (AID::dTagmB>F>P::::KNL-1))III ; unc-119(ed3)III?; unc-119 (ed3)III; dhaSi53[oxTi177;pDC675; Pdes-2::Mng-PH::unc-54 3'UTR; cb-unc-119 (+)]IV clone B; dhaSi237[oxTi177; pDC1061;Pser-2prom3::mscarlet::linker::LGG1:unc 54 3'UTR; cb-unc-119(+)]V #1*	This study	DKC1131
dma-1 (dha155; DEL)I	This study	DKC919

Table S2. CRISPR-Cas9 Protocol & sgRNA Sequences Used for Strain Generation

GENOTYPE	**METHOD & REFERENCE**	**sgRNA SEQUENCE**
knl-1(dha122 (AID::dTagmB>F>P::::KNL-1))III &knl-1(dha130; HA::7XGFP11::knl-1)III	Ribonucleoprotein complex (Paix, et al., 2015)	catatttacagccATGTCGA & CTTACGAGGCTCCATCGACA
dhaSi76[ndc-80(dha148; NDC-80::AID::dgfp^3XFLAG)	SEC (Dickinson et al., 2015)	ATGTGCTGGCATTGAAAAGG
dma-1 (dha155; DEL)I	Ribonucleoprotein complex (Paix, et al., 2015)	agctagaagcagcaaacgtg & GGTGCTGGTGGAATCAATGG

REFERENCES

1. Jan, Y.N., and Jan, L.Y. (2001). Dendrites. Genes Dev. *15*, 2627–2641.

2. Jan, Y.N., and Jan, L.Y. (2010). Branching out: mechanisms of dendritic arborization. Nat. Rev. Neurosci. *11*, 316–328.

3. Li, Z., Van Aelst, L., and Cline, H.T. (2000). Rho GTPases regulate distinct aspects of dendritic arbor growth in Xenopus central neurons in vivo. Nat. Neurosci. *3*, 217–225.

4. Luo, L., Hensch, T.K., Ackerman, L., Barbel, S., Jan, L.Y., and Jan, Y.N. (1996). Differential effects of the Rac GTPase on Purkinje cell axons and dendritic trunks and spines. Nature *379*, 837–840.

5. Threadgill, R., Bobb, K., and Ghosh, A. (1997). Regulation of dendritic growth and remodeling by Rho, Rac, and Cdc42. Neuron *19*, 625–634.

6. Nakayama, A.Y., Harms, M.B., and Luo, L. (2000). Small GTPases Rac and Rho in the maintenance of dendritic spines and branches in hippocampal pyramidal neurons. J. Neurosci. *20*, 5329–5338.

7. Scott, E.K., and Luo, L. (2001). How do dendrites take their shape? Nat. Neurosci. *4*, 359–365.

8. Lefebvre, J.L. (2021). Molecular mechanisms that mediate dendrite morphogenesis. Curr. Top. Dev. Biol. *142*, 233–282.

9. Sundararajan, L., Stern, J., and Miller, D.M., 3rd (2019). Mechanisms that regulate morphogenesis of a highly branched neuron in C. elegans. Dev. Biol. *451*, 53–67.

10. Taylor, C.A., Yan, J., Howell, A.S., Dong, X., and Shen, K. (2015). RAB-10 Regulates Dendritic Branching by Balancing Dendritic Transport. PLoS Genet. *11*, e1005695.

11. Maniar, T.A., Kaplan, M., Wang, G.J., Shen, K., Wei, L., Shaw, J.E., Koushika, S.P., and Bargmann, C.I. (2012). UNC-33 (CRMP) and ankyrin organize microtubules and localize kinesin to polarize axon-dendrite sorting. Nat. Neurosci. *15*, 48–56.

12. Jaworski, J., Kapitein, L.C., Gouveia, S.M., Dortland, B.R., Wulf, P.S., Grigoriev, I., Camera, P., Spangler, S.A., Di Stefano, P., Demmers, J., et al. (2009). Dynamic microtubules regulate dendritic spine morphology and synaptic plasticity. Neuron *61*, 85–100.

13. Cao, Y., Lipka, J., Stucchi, R., Burute, M., Pan, X., Portegies, S., Tas, R., Willems, J., Will, L., MacGillavry, H., et al. (2020). Microtubule Minus-End Binding Protein CAMSAP2 and Kinesin-14 Motor KIFC3 Control Dendritic Microtubule Organization. Curr. Biol. *30*, 899-908.e6.

14. Kahn, O.I., Schätzle, P., van de Willige, D., Tas, R.P., Lindhout, F.W., Portegies, S., Kapitein, L.C., and Hoogenraad, C.C. (2018). APC2 controls dendrite development by promoting microtubule dynamics. Nat. Commun. *9*, 2773.

15. Nguyen, M.M., McCracken, C.J., Milner, E.S., Goetschius, D.J., Weiner, A.T., Long, M.K., Michael, N.L., Munro, S., and Rolls, M.M. (2014). Γ-tubulin controls neuronal microtubule polarity independently of Golgi outposts. Mol. Biol. Cell *25*, 2039–2050.

16. Merriam, E.B., Lumbard, D.C., Viesselmann, C., Ballweg, J., Stevenson, M., Pietila, L., Hu, X., and Dent, E.W. (2011). Dynamic microtubules promote synaptic NMDA receptor-dependent spine enlargement. PLoS One *6*, e27688.

17. Hu, X., Viesselmann, C., Nam, S., Merriam, E., and Dent, E.W. (2008). Activity-dependent dynamic microtubule invasion of dendritic spines. J. Neurosci. *28*, 13094–13105.

18. Cheerambathur, D.K., and Desai, A. (2014). Linked in: formation and regulation of microtubule attachments during chromosome segregation. Curr. Opin. Cell Biol. *26*, 113–122.

19. Musacchio, A., and Desai, A. (2017). A Molecular View of Kinetochore Assembly and Function. Biology *6*, 5.

20. Cheerambathur, D.K., Prevo, B., Chow, T.-L., Hattersley, N., Wang, S., Zhao, Z., Kim, T., Gerson-Gurwitz, A., Oegema, K., Green, R., et al. (2019). The Kinetochore-Microtubule Coupling Machinery Is Repurposed in Sensory Nervous System Morphogenesis. Dev. Cell *48*, 864-872.e7.

21. Zhao, G., Oztan, A., Ye, Y., and Schwarz, T.L. (2019). Kinetochore Proteins Have a Post-Mitotic Function in Neurodevelopment. Dev. Cell *48*, 873-882.e4.

22. Hertzler, J.I., Simonovitch, S.I., Albertson, R.M., Weiner, A.T., Nye, D.M.R., and Rolls, M.M. (2020). Kinetochore proteins suppress neuronal microtubule dynamics and promote dendrite regeneration. Mol. Biol. Cell *31*, 2125–2138.

23. Smith, C.J., Watson, J., Spencer, W.C., O'Brien, T., Cha, B., Albeg, A., Treinin, M., and Miller, D.M., III (2010). Time-lapse imaging and cell-specific expression profiling reveal dynamic branching and molecular determinants of a multi-dendritic nociceptor in C. elegans. Dev. Biol. *345*, 18–33.

24. Kamiyama, D., Sekine, S., Barsi-Rhyne, B., Hu, J., Chen, B., Gilbert, L.A., Ishikawa, H., Leonetti, M.D., Marshall, W.F., Weissman, J.S., et al. (2016). Versatile protein tagging in cells with split fluorescent protein. Nat. Commun. *7*, 929.

25. Nishimura, K., Fukagawa, T., Takisawa, H., Kakimoto, T., and Kanemaki, M. (2009). An auxin-based degron system for the rapid depletion of proteins in nonplant cells. Nat. Methods *6*, 917–922.

26. Ashley, G.E., Duong, T., Levenson, M.T., Martinez, M.A.Q., Johnson, L.C., Hibshman, J.D., Saeger, H.N., Palmisano, N.J., Doonan, R., Martinez-Mendez, R., et al. (2021). An expanded auxin-inducible degron toolkit for Caenorhabditis elegans. Genetics *217*. 10.1093/genetics/iyab006.

27. Liao, C.-P., Li, H., Lee, H.-H., Chien, C.-T., and Pan, C.-L. (2018). Cell-Autonomous Regulation of Dendrite Self-Avoidance by the Wnt Secretory Factor MIG-14/Wntless. Neuron *98*, 320-334.e6.

28. E, L., Zhou, T., Koh, S., Chuang, M., Sharma, R., Pujol, N., Chisholm, A.D., Eroglu, C., Matsunami, H., and Yan, D. (2018). An Antimicrobial Peptide and Its Neuronal Receptor Regulate Dendrite Degeneration in Aging and Infection. Neuron *97*, 125-138.e5.

29. He, L., Kooistra, R., Das, R., Oudejans, E., van Leen, E., Ziegler, J., Portegies, S., de Haan, B., van Regteren Altena, A., Stucchi, R., et al. (2020). Cortical anchoring of the microtubule cytoskeleton is essential for neuron polarity. Elife *9*. 10.7554/eLife.55111.

30. He, L., van Beem, L., Snel, B., Hoogenraad, C.C., and Harterink, M. (2022). PTRN-1 (CAMSAP) and NOCA-2 (NINEIN) are required for microtubule polarity in Caenorhabditis elegans dendrites. PLoS Biol. *20*, e3001855.

31. Harterink, M., Edwards, S.L., de Haan, B., Yau, K.W., van den Heuvel, S., Kapitein, L.C., Miller, K.G., and Hoogenraad, C.C. (2018). Local microtubule organization promotes cargo transport in C. elegans dendrites. J. Cell Sci. *131*, jcs223107.

32. Zou, W., Dong, X., Broederdorf, T.R., Shen, A., Kramer, D.A., Shi, R., Liang, X., Miller, D.M., III, Xiang, Y.K., Yasuda, R., et al. (2018). A Dendritic Guidance Receptor Complex Brings Together Distinct Actin Regulators to Drive Efficient F-Actin Assembly and Branching. Dev. Cell *45*, 362-375.e3.

33. Tang, L.T., Diaz-Balzac, C.A., Rahman, M., Ramirez-Suarez, N.J., Salzberg, Y., Lázaro-Peña, M.I., and Bülow, H.E. (2019). TIAM-1/GEF can shape somatosensory dendrites independently of its GEF activity by regulating F-actin localization. Elife *8*. 10.7554/eLife.38949.

34. Yan, J., Chao, D.L., Toba, S., Koyasako, K., Yasunaga, T., Hirotsune, S., and Shen, K. (2013). Kinesin-1 regulates dendrite microtubule polarity in Caenorhabditis elegans. Elife *2*, 153.

35. Sundararajan, L., Smith, C.J., Watson, J.D., Millis, B.A., Tyska, M.J., and Miller, D.M., 3rd (2019). Actin assembly and non-muscle myosin activity drive dendrite retraction in an UNC-6/Netrin dependent self-avoidance response. PLoS Genet. *15*, e1008228.

36. Cheng, L., Zhang, J., Ahmad, S., Rozier, L., Yu, H., Deng, H., and Mao, Y. (2011). Aurora B regulates formin mDia3 in achieving metaphase chromosome alignment. Dev. Cell *20*, 342–352.

37. Mogessie, B., and Schuh, M. (2017). Actin protects mammalian eggs against chromosome segregation errors. Science *357*. 10.1126/science.aal1647.

38. Yasuda, S., Oceguera-Yanez, F., Kato, T., Okamoto, M., Yonemura, S., Terada, Y., Ishizaki, T., and Narumiya, S. (2004). Cdc42 and mDia3 regulate microtubule attachment to kinetochores. Nature *428*, 767–771.

39. Harasimov, K., Uraji, J., Mönnich, E.U., Holubcová, Z., Elder, K., Blayney, M., and Schuh, M. (2023). Actin-driven chromosome clustering facilitates fast and complete chromosome capture in mammalian oocytes. Nat. Cell Biol. 10.1038/s41556-022-01082-9.

40. Frøkjaer-Jensen, C., Davis, M.W., Hopkins, C.E., Newman, B.J., Thummel, J.M., Olesen, S.-P., Grunnet, M., and Jorgensen, E.M. (2008). Single-copy insertion of transgenes in Caenorhabditis elegans. Nat. Genet. *40*, 1375–1383.

41. Dickinson, D.J., Ward, J.D., Reiner, D.J., and Goldstein, B. (2013). Engineering the Caenorhabditis elegans genome using Cas9-triggered homologous recombination. Nat. Methods *10*, 1028–1034.

42. Waaijers, S., Portegijs, V., Kerver, J., Lemmens, B.B.L.G., Tijsterman, M., van den Heuvel, S., and Boxem, M. (2013). CRISPR/Cas9-Targeted Mutagenesis in Caenorhabditis elegans. Genetics *195*, 1187–1191.

43. Paix, A., Folkmann, A., Rasoloson, D., and Seydoux, G. (2015). High Efficiency, Homology-Directed Genome Editing in Caenorhabditis elegansUsing CRISPR-Cas9 Ribonucleoprotein Complexes. Genetics *201*, 47–54.

44. Gibson, D.G., Young, L., Chuang, R.-Y., Venter, J.C., Hutchison, C.A., and Smith, H.O. (2009). Enzymatic assembly of DNA molecules up to several hundred kilobases. Nat. Methods *6*, 343–345.

45. Mangeol, P., Prevo, B., and Peterman, E.J.G. (2016). KymographClear and KymographDirect: two tools for the automated quantitative analysis of molecular and cellular dynamics using kymographs. Mol. Biol. Cell *27*, 1948–1957.